**Noname manuscript No.**
(will be inserted by the editor)

# Scenarios in the experimental response of a vibro-impact single-degree-of-freedom system and numerical simulations

**Giulia Stefani · Maurizio De Angelis · Ugo Andreaus**

Received: date / Accepted: date

**Abstract** In this paper, possible scenarios within the experimental dynamic response of a vibro-impact single-degree-of-freedom (SDOF) system, symmetrically constrained by deformable and dissipative bumpers, were identified and described. The different scenarios were obtained varying selected parameters, namely peak value of table acceleration A, amplitude of the total gap between mass and bumpers G and bumper's stiffness B. Subsequently, using a Simplified Nonlinear Model (SNM), results in good agreement with the experimental outcomes were obtained, although the model includes only the nonlinearities due to clearance existence and impact occurrence. Further numerical analysis highlighted other scenarios that can be obtained for values of the parameters not considered in the experimental laboratory campaign. Finally, to attempt a generalization of the results, suitable dimensionless parameters were introduced.

**Keywords** Non-smooth dynamics · Vibro-impact SDOF system · Double-sided deformable and dissipative constraints · Experimental tests · Numerical model · Scenarios

## 1 Introduction

The problem of impact is ubiquitous in many practical (biomedical, mechanical, civil, ...) engineering applications involving mechanical components or structures repeatedly colliding with one another or with obstacles [1]. Impacts occur, for example, in the capsule systems used in clinic endoscopy to inspect the surface lining of the intestine in the human body. The dynamics of this system is the subject of several works, of both numerical and experimental nature [2–6]. In these studies the endoscopy capsule is modelled by a two-degree-of-freedom system, consisting of rigid capsule and a movable internal mass, the latter driven by a harmonic force with one-sided or two-sided constraints. In this system impact occurs when the relative displacement of the internal mass and the capsule exceeds the gap between them. Non-smooth dynamics is observed also in the drilling rig used in the oil and gas industry for creation of the wells [7–12]. During drilling, the interaction between the drill-string, the fundamental part of the rig, and the rock, is characterized by alternating contact and noncontact phases that cause detrimental axial, torsional and flexural vibrations.

In the context of structural pounding, the occurrence of exceptional loads, like severe earthquakes, can produce large horizontal displacements in base-isolated structures. If the large displacements cannot be accommodated through adequate gaps, they can lead to pounding with the surrounding moat walls or adjacent structures. The consequences of pounding can range from local to severe structural damage [13–19]. Furthermore, the acceleration spikes, produced by the impacts, can damage sensitive equipment housed in the structures [20, 21] and impair their functionality. Pounding is a problem that also affects other systems like strategic facilities [22] and bridges [23–25]. When it is not possible to guarantee a sufficient seismic gap, the side effects induced by the occurrence of impacts can be mitigated reducing the impact stiffness through the interposition of dissipative and deformable shock absorbers (also known

G. Stefani · M. De Angelis · U. Andreaus
Department of Structural and Geotechnical Engineering, Sapienza University of Rome
Via Eudossiana 18, 00184 Rome, Italy
E-mail: giulia.stefani@uniroma1.it

as bumpers) between the colliding systems. Anagnostopoulos [26] investigated the effects of pounding in several adjacent buildings due to strong earthquakes and found that the interposition of soft viscoelastic material between two adjacent structures can reduce the effects of pounding significantly. The effectiveness of rubber bumpers as mitigation measure for pounding of seismically isolated buildings was numerically investigated in [27,28]. Even in the absence of obstacles, there may be a need to limit the displacements, so as to avoid the damage of the isolation system. This objective could be achieved either by inserting suitable obstacles or by using other types of control systems [29,30].

Several scientific works, of both numerical and experimental nature, dealt with vibro-impact dynamics. In the numerical simulations impact can be modelled using both a steromechanical or a force-based approach [31]. In the first approach, the duration of the contact is neglected and the impact is modelled using the momentum conservation principle and the coefficient of restitution, the latter defined as the ratio between the post- and the pre-impact velocities [32]. In the second approach, the contact force can be modelled in different ways, resorting to more or less sophisticated modelling [33–37]. The simplest model is represented by the linear spring element, which assumes a linear relation between the contact force and the penetration, not taking into account the energy loss during the impact. Another well-known contact force model, which, in turn, does not account for energy dissipation, is the Hertz contact model [38,39], represented by a nonlinear spring element, in which the contact force is expressed as a nonlinear power function of the penetration. In order to overcome the limitations of the pure elastic contact force models, dissipative contact force models were proposed to take into account the energy loss during the contact process. Among these, one of the first proposed was the Kelvin-Voigt model which combines a linear spring with a linear damper, arranged in parallel [32]. The existence of the damping component causes that, at the beginning of the contact process, the damping force is not null. Furthermore, at the end of the restitution phase, the relative velocity, and thus the contact force, is negative meaning that the colliding bodies attract each other, but this does not make sense from a physical point of view. Another limitation of the model, not fully consistent with reality, is that the assumption of a constant damping coefficient results in a uniform dissipation during the impact time interval. Despite these weaknesses, the Kelvin and Voigt model has been used by a several researchers [40,41]. To overcome the drawbacks of the Kelvin-Voigt model, Hunt and Crossley [42] proposed a contact force model in which the elastic Hertz's law is combined with a nonlinear viscoelastic element (Hertzdamp model). Since the damping term is expressed as a function of indentation, the contact force is null both at the beginning and at the end of the contact process.

There are several works in which the types of motion and bifurcations that can occur in the dynamics of vibro-impact systems, with the variation of selected parameters, are investigated. Wagg and Bishop [43] investigated the dynamics of a two-degree-of-freedom impact oscillator with motion limiting constraint, and highlighted a range of periodic and nonperiodic impact motions. They studied the bifurcations which occur between differing regimes of impacting motion, in particular those which occur due to a grazing bifurcation, the periodic and chaotic chatter motions and the regions of sticking. The dynamics of impact oscillators with multiple degrees of freedom subject to more than one motion limiting constraint and the possible impact configurations were investigated by the same authors in [44]. Then, considering a two-degree-of-freedom system with two constraints, they used bifurcation diagrams to indicate differing regimes of vibro-impacting motion for two different constraint configurations. Rigaud and Perret-Liaudet [45] investigated the experimental and numerical dynamic responses of a double sphere-plane preloaded Hertzian dry contact, excited by a purely harmonic input normal force and obtained typical response curves for several input levels. Luo et al. [46] considered a two-degree-of-freedom system with a clearance subjected to harmonic excitation and investigated the influence of the exciting frequency and clearance on dynamic performance of the system. They defined the fundamental group of impact motions and studied the transitions from one motion to the other, which basically goes through different types of bifurcations, and the occurrence of chattering-impact vibration. The generation mechanism of complete and incomplete chattering-impact vibration of the system was investigated in [47]. Luo and Wang [48] studied the dynamics of a two-degree-of-freedom periodically-forced system with symmetric motion limiting constraints, with emphasis on the mutual transition characteristics between neighboring regions of fundamental impact motions and designed and realized an electronic circuit for physical implementation of dynamics of the system. Hao et al. [49] proposed a two-sided damping constraint control strategy to improve the performance of the quasi-zero stiffness (QZS) isolator for both low- and high-frequency components simultaneously and to prevent the severity of end-stop impact. From the analysis of two-parameter bifurcation diagrams and basins of attraction, they found that the key factor to realize such control objective

is to suppress the period-3 solutions that coexist with the desired small amplitude period-1 motions. Wang et al. [50] investigated the dynamical behavior of a single degree-of-freedom impact oscillator that impacts at one stop and is shocked with impulse excitation at the other stop and established the existing and stability conditions for period-1 motion of the oscillator and its properties. Furthermore, they discussed the effects of system parameters on dynamical response under different initial velocities. The nonlinear dynamic behavior of a one-degree-of-freedom impact oscillator with a single rigid constraint and controlled with an OGY-based state-feedback control law was investigated by Gritli and Belghith [51], through bifurcation diagrams. Using a hybrid Poincaré map, they illustrated, through time-traces, phase portraits and Poincaré sections, the occurrence of several behaviors, including the period-doubling route to chaos, the period-adding cascade, interior and boundary crisis, the complete and incomplete chaotic chattering, the cyclic-fold bifurcation, the saddle-saddle bifurcation, the NeimarkSacker bifurcation, the sub-critical period-doubling bifurcation, the grazing bifurcation and the border-collision bifurcation. The response of a single-degree-of-freedom vibro-impact model with the coefficient of restitution was studied by de S. Rebouças et al. [52]. The authors investigated the experimental response of a cantilever beam with unilateral constraint, different gap configurations and levels of excitation, highlighted different qualitative behaviors near vibro-impact resonance and used numerical simulations to reproduce experimental observations.

The practical problem of base-isolated structures impacting against moat-walls inspired several works of the Authors, of both numerical and experimental nature, in which the response of these structures was simulated using a single-degree-of-freedom (SDOF) oscillator, consisting of a mass isolated by means of an isolator and impacting against two deformable and dissipative constraints (bumpers), symmetrically arranged on the sides. In the theoretical-numerical study presented by Andreaus and De Angelis in [53], the analysis of the system's dynamic response allows the Authors to highlight the presence of hysteresis ranges, jumps between multi-periodic orbits, and super-harmonics and to observe how unilateral constraints modify the response of the SDOF oscillator with respect to the absence of bumpers. This numerical investigation guided subsequent experimental parametric laboratory campaigns [54,55], conducted on a small scale physical model of the system using the shaking table and considering different bumpers, gaps amplitudes, and table accelerations. The influence of geometrical and mechanical characteristics of isolation and mitigation devices on the nonlinear non-smooth response of vibro-impact systems was experimentally and numerically investigated in [56]. Suitable choices of pairs of bumpers and gaps, that allows to reach a trade-off between two conflicting objectives, namely, control of excessive displacements and control of excessive accelerations were suggested in [57] and a numerical model was proposed in order to simulate the experimental results. In [58] Stefani et al. focused the attention on the experimental pseudo-resonance curves of maximum absolute acceleration and excursion of the SDOF oscillator and characterized the hysteresis zone between the jumps. Some characteristics of the dynamics with impact, evaluated from the experimental results, namely force and time of contact between mass and bumpers, coefficient of restitution and energy dissipated by the bumpers during the impact were presented and discussed in [59]. In [60], referring to the experimental results relating to one of the considered bumpers, different scenarios that can occur in the system's experimental response, varying the investigated parameters, were highlighted and described. Those scenarios were reproduced also numerically using a Simplified Nonlinear Model (SNM), described in terms of dimensionless parameters.

The present work represents a deepening and an extension of the study presented in [60], the latter limited to one of the considered bumpers. In this paper attention is devoted to the identification and characterization of possible scenarios that can occur in the experimental response of the vibro-impact single-degree-of-freedom (SDOF) system, symmetrically constrained with deformable and dissipative bumpers, varying the peak value of table acceleration A, the amplitude of the total gap between mass and bumpers G and the bumper's stiffness B. Based on the experimental results, the parameters of a Simplified Nonlinear Model (SNM) were identified in order to reproduce the experimental scenarios. In this model both the behaviors of the bumpers and the damper were modelled using a Kelvin-Voigt model, retaining the other sources of nonlinearity, namely the existence of clearances, the unilaterality of the contact and the occurrence of impact, which causes abrupt changes of stiffness and damping at the contact time. Using the same model, further numerical analyses were carried out in order to integrate the experimental results and highlight the existence of other possible scenarios. Finally, in order to attempt a generalizations of the obtained results, suitable dimensionless parameters were introduced. The authors are aware of the limitations of the Kelvin-Voigt model; however, they consider this model satisfactory for the purposes of this work.

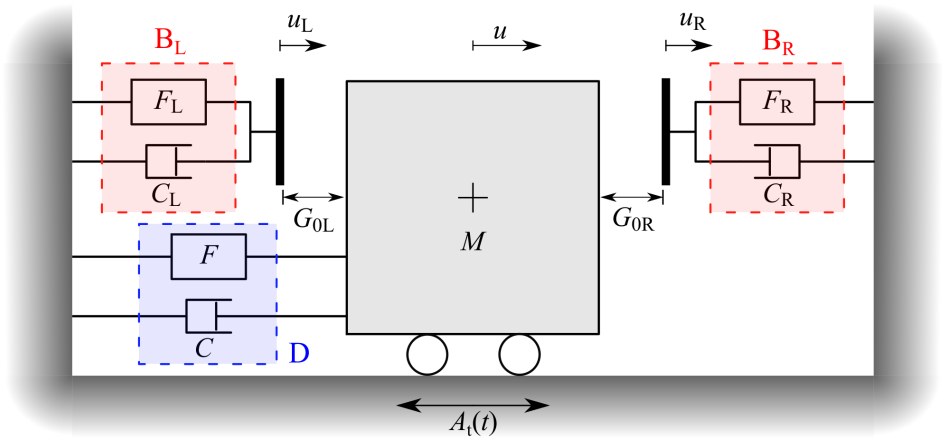


**Fig. 1** Model of the SDOF system.

As emerges from the scientific Literature on this topic, there are not many works that in a such systematic way, resorting both to experimental and numerical investigations, and using different synthetic representations, frame and classify the scenarios that can occur, in the dynamic non-smooth response of a vibro-impact SDOF system.

The paper is organized as follows. The numerical model of the system and the equations of motion are introduced in Section 2; the physical model and the experimental tests are described in Section 3; in Section 4 some of the experimental results and the identified scenarios are shown and discussed; the identification of the parameters of the Simplified Nonlinear Model (SNM) and the comparison between experimental and numerical results are presented in Section 5; in Section 6 further numerical scenarios, obtained for values of the parameters not experimentally investigated, are presented and discussed; suitable dimensionless parameters and a rereading of the results according to these parameters are given in Section 7; the main conclusions and future developments are drawn in Section 8.

## 2 Model and Equations of motion

The numerical model of the SDOF oscillator is shown in Figure 1. It consists of a mass $M$, a damper (D) and two bumpers, denoted as right bumper ($B_R$) and left bumper ($B_L$) respectively, symmetrically arranged on the two sides of the mass. The system is subject to a base excitation $A_t(t)$.

During the motion, the system can be in three configurations. The corresponding equations of motion are:

– The mass is not in contact with any of the bumpers (flight):

$$M\ddot{u}(t) + C\dot{u}(t) + F(t) = -MA_t(t) \quad (1a)$$
$$C_j\dot{u}_j(t) + F_j(t) = 0; \quad G_j(t) > 0 \quad (j = R,L) \quad (1b)$$

– The mass is in contact with the right bumper:

$$M\ddot{u}(t) + C\dot{u}(t) + F(t) + C_R\dot{u}_R(t) + F_R(t) = -MA_t(t) \quad (2a)$$
$$C_L\dot{u}_L(t) + F_L(t) = 0; \quad G_R(t) = 0 \quad (2b)$$

– The mass is in contact with the left bumper:

$$M\ddot{u}(t) + C\dot{u}(t) + F(t) + C_L\dot{u}_L(t) + F_L(t) = -MA_t(t) \quad (3a)$$
$$C_R\dot{u}_R(t) + F_R(t) = 0; \quad G_L(t) = 0 \quad (3b)$$

where $u(t)$ and $u_j(t)$ (j = R, L) are the relative displacements of the mass and of the bumpers respectively with respect to the ground and the dot $(\cdot)$ denotes differentiation with respect to the time $t$. $C$ and $C_j$ (j = R, L) are the damping coefficients of the damper and the bumpers respectively; $F(t)$ and $F_j(t)$ (j = R, L) are the restoring forces exerted by the damper and the bumpers respectively. $G_j(t)$ (j = R, L) is the clearance function which represents the distance, instant by instant, between the mass and the $j$-th bumper:

$$G_j(t) = G_{0j} + \Delta u_j(t) \quad (j = R,L) \quad (4a)$$
$$\Delta u_R(t) = u_R(t) - u(t); \quad \Delta u_L(t) = u(t) - u_L(t) \quad (4b)$$

where $G_{0j}$ (j = R, L) is the $j$-th initial gap, that is the initial distance between the mass and the $j$-th bumper. When the mass is in contact with the $j$-th bumper $G_j(t) = 0$, otherwise $G_j(t) > 0$. In this study we considered two equal bumpers symmetrically positioned on

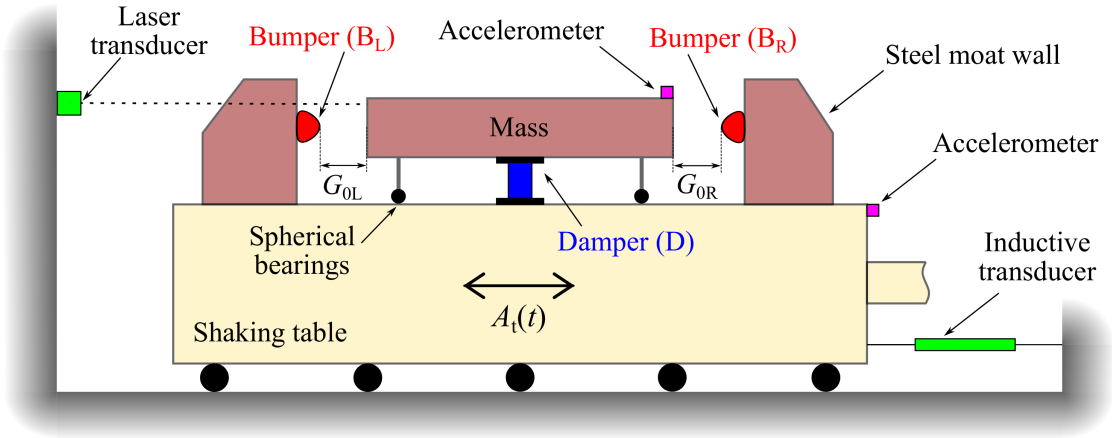


**Fig. 2** Schematic view of the experimental setup.

the two sides of the mass. Thus, it is $F_R = F_L$, $C_R = C_L$ and $G_{0R} = G_{0L}$.

The studied physical model is strongly nonlinear. Nonlinearities are due to the behavior of damper and bumpers, the gap, the unilateral constrains and the impact that induces abrupt changes of both stiffness and damping.

## 3 Experimental setup

The physical model of the system consists of a rigid body (mass $M = 550$ kg), an elastomeric high damping rubber bearing (HDRB) isolator (damper), and a couple of symmetrically mounted elastomeric shock absorbers (bumpers placed on steel moat walls), as shown in Figure 2.

The system was excited by a step-wise forward ($f = 0.5 - 5$ Hz with $\Delta f = 0.1$ Hz) and backward ($f = 5 - 0.5$ Hz with $\Delta f = 0.1$ Hz) sine sweep in displacement control, in order to impose a given peak acceleration A, with a number of cycles such as to reach the steady state condition. The attainment of the steady state condition was checked by verifying the convergence to the limit cycle in both planes of phase portraits and hysteresis loops. Two configurations, with and without bumpers, under the same base excitation, were considered [56].

The experimental tests were carried out to investigate the influence on the system response of selected parameters, namely:

- peak table acceleration Ai (i = 1, 2, 3); in particular A1 = $0.03g$, A2 = $0.04g$, A3 = $0.05g$, where $g$ is the gravity's acceleration;
- amplitude of the total gap Gj (j = 1, 2, 3, 4 and G$\infty$) between mass and bumpers, defined as the sum of right $G_{0R}$ and left $G_{0L}$ gaps (Figure 2); in particular G1 = 15 mm, G2 = 20 mm, G3 = 25 mm, G4 = 30 mm and G$\infty$ denotes all the situations in which the gap is large enough not to have the impact between the mass and the bumpers; this occurs both in the free flight condition (absence of bumpers) and when the mass just grazes the bumpers; in the latter case, the corresponding value of G$\infty$ depends on A;
- bumper's stiffness Bk (k = 1, 2, 3, 4); the stiffness of the bumper increases as k increases.

In the experimental laboratory campaign, each performed test corresponds to a combination of these three parameters.

The measured parameters during the tests were the absolute accelerations and displacements of the mass and of the shaking table. The accelerations were measured by accelerometers and the displacements were measured by a laser transducer, for what concerns the mass, and by an inductive transducer, for what concerns the shaking table (Figure 2).

For a more detailed description of the experimental setup see [57].

## 4 Experimental results

In this Section the experimental results, represented in terms of forward and backward Pseudo-Resonance Curves (PRCs) of normalized excursion of absolute acceleration ($\eta_a = E_a/E_{a,flight,max}$) and relative displacement ($\eta_d = E_d/E_{d,flight,max}$) of the mass, are discussed. The excursion $E$ was calculated as the difference between the maximum and minimum values recorded at steady-state of each sub-frequency range. Subsequently, these excursions $E$ were normalized with respect to the maximum excursion in the backward sweep in free flight condition ($E_{flight,max}$). Based on this normalization, a value of normalized excursion $\eta$ greater than 1 means

that in presence of bumpers the excursion is larger compared to the free flight condition.

### 4.1 Free flight condition

In the free flight condition, that is when the mass is free to move without obstacles, forward (in the following Figures identified with the letter (f) in the legend) and backward (in the following Figures indicated with the letter (b) in the legend) PRCs of the excursion of absolute acceleration ($E_a$) and relative displacement ($E_d$) of the mass, show a softening behavior, due to the damper, gradually more evident as the excitation amplitude A increases.

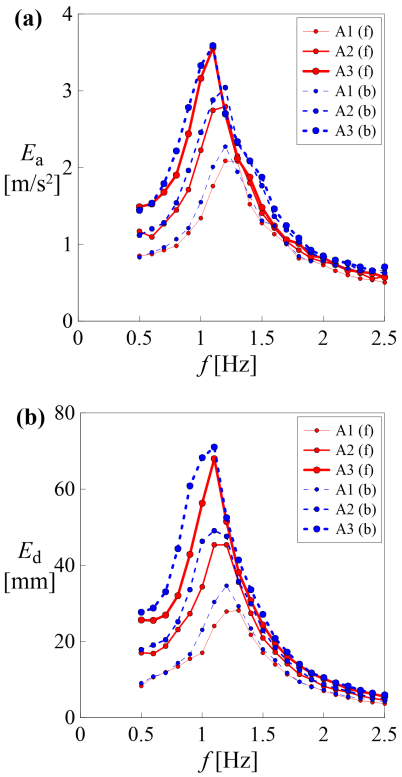


**Fig. 3** Free flight condition: a) $E_a$[m/s$^2$]; b) $E_d$[mm].

As shown in Figure 3, as A increases (increasing thickness of the lines and size of the markers), the maximum values of excursion, of both absolute acceleration and relative displacement, increase and resonance occurs for decreasing values of frequency. As can be seen from the same Figures, even in the case of the maximum amplitude of the excitation considered in the laboratory campaign (A3), the extension of the hysteresis is limited.

### 4.2 Contact condition

When impact occurs, the PRCs bend to the right (Figures 4(b) and 4(c)) due to the hardening caused by impact against the bumpers, as it can be seen in Figure 4(a), in which the absolute acceleration *vs* relative displacement cycles, in steady-state forward resonance condition, corresponding to the absence (free flight, black curve) and presence of bumper (red curve, corresponding to the combination B4-G4-A3) are compared.

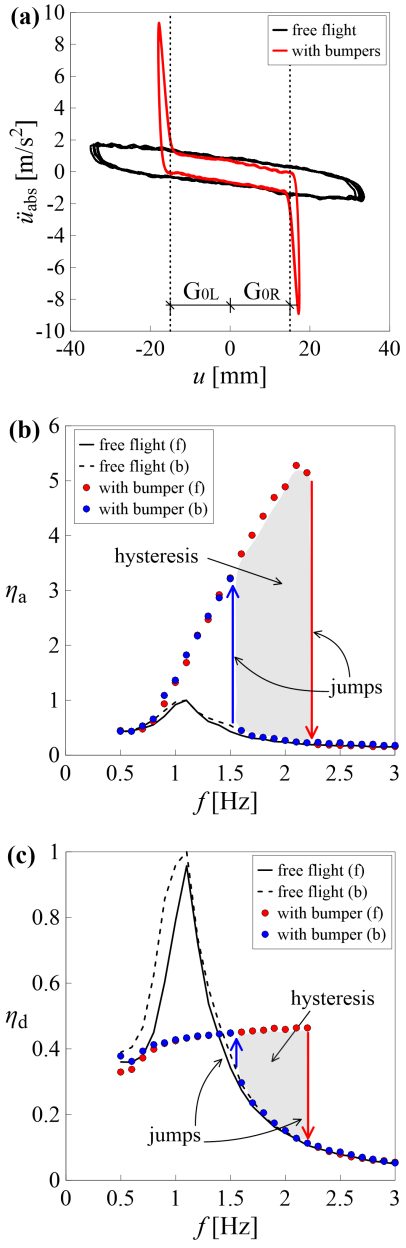


**Fig. 4** Comparison between free flight and contact (B4-G4-A3) condition: a) absolute acceleration *vs* relative displacement cycle; b) $\eta_a$; c) $\eta_d$.

In Figures 4(b) and 4(c), the same comparison is made in terms of PRCs of normalized excursion of absolute acceleration $\eta_{\mathrm{a}}$ (Figure 4(b)) and relative displacement $\eta_{\mathrm{d}}$ (Figure 4(c)). In these Figures, the PRCs corresponding to the free flight condition are represented with solid (forward sweep) and dashed (backward sweep) black lines, whereas the PRCs representative of the contact condition (combination B4-G4-A3) are represented with red (forward sweep) and blue (backward sweep) markers.

By increasing the excitation frequency (red markers, forward sweep), the amplitude of the response increases, initially overlapping the curve in free flight, until impact occurs; subsequently, the response continues to increase, following a different path until a sudden downward jump (represented with a vertical red arrow pointing downwards) to a smaller amplitude response (associated with the absence of impact) occurs and then continues to decrease slowly, overlapping the curve in free flight.

If the exciting frequency is decreased (blue markers, backward sweep), the amplitude of the response increases slowly, overlapping the curve in free flight, until a sudden upward jump (represented with a vertical blue arrow pointing upwards) to a larger amplitude response (associated with the occurrence of impact) occurs and then continues to decrease, following the corresponding forward curve.

The presence of jumps give rise to an hysteresis in the $\eta$ *vs* $f$ plane (*primary resonance with right hysteresis*), highlighted in Figures 4(b) and 4(c) with a light grey shaded area. In the frequency interval between the two jumps, for each value of frequency there are three steady-state solutions, two stable, corresponding respectively to large and small amplitude oscillations, and one unstable and thus not experimentally reproducible.

In following Figures 5 and 6 the forward (solid lines) and backward (dashed lines) PRCs, respectively of normalized excursion of absolute acceleration $\eta_a$ (Figure 5) and relative displacement $\eta_d$ (Figure 6) of the mass, are represented for different values of the total gap G (each color corresponds to a gap amplitude). The sub-figures belonging to the same column of the grid are characterized by the same value of peak table acceleration A, while the sub-figures belonging to the same row of the grid correspond to the same bumper B.

From Figure 5 it can be observed that, compared to the free flight condition, in presence of bumpers $\eta_a$ is always greater than 1, both in the forward and in the backward sweeps, with the amplitude of the forward resonance greater than that of the backward resonance.

For a given pair B-A, which corresponds to a sub-figure in Figure 5 (for example B2-A3), compared to the free flight condition, as the total gap G decreases, the jump frequencies, both in the forward and in the backward sweeps, the latter to a lesser extent, increase. For the selected B-A pair, the maximum values of excursion, both in the forward and in the backward resonance condition, the latter to a lesser extent, show a bell-shaped trend. For other combinations of B and A, it is possible to capture only the ascending branch (see for example the sub-figure corresponding to B1-A1) or only the descending branch (see for example the sub-figure corresponding to B4-A3) of the envelope of the maxima. Furthermore, decreasing the total gap, secondary resonances in the low frequency range appear.

For a given pair B-G (see for example the second row of sub-figures, associated with the bumper B2 and focus the attention on the curves corresponding for example to the total gap G1), increasing the table acceleration , that is moving from the left column to the right column, it can be observed that the jump frequencies, both in the forward and in the backward sweeps, the latter to a lesser extent, increase. The maximum values of excursion in the forward resonance condition increase, while the maximum values of excursion in the backward resonance condition increase to a lesser extent. Furthermore, increasing the table acceleration, secondary resonances in the low frequency range appear.

With the same acceleration A and total gap G (see for example the third column of sub-figures, associated with the acceleration A3 and focus the attention on the curves corresponding to the total gap G1), increasing the bumper stiffness, that is moving from the top row to the bottom row, it can be observed that the jump frequencies, both in the forward and in the backward sweeps, the latter to a lesser extent, increase. The maximum values of excursion both in the forward and in the backward resonance condition increase. Furthermore, increasing the stiffness of the bumper, secondary resonances in the low frequency range appear. It can also be observed that bumpers B2 and B3 behave in a similar way.

From Figure 5, it can also be observed that in the case of the combination of the most deformable bumper with the smallest table acceleration (pair B1-A1, top left corner of the Figure) PRCs are quite similar to those associated with the free flight condition, while the difference becomes more evident for the pair characterized by the stiffest bumper and the greatest table acceleration (pair B4-A3, lower right corner of the Figure).

Finally, a fixed point for $f \simeq 1$Hz can be observed, especially for the higher values of B and A.

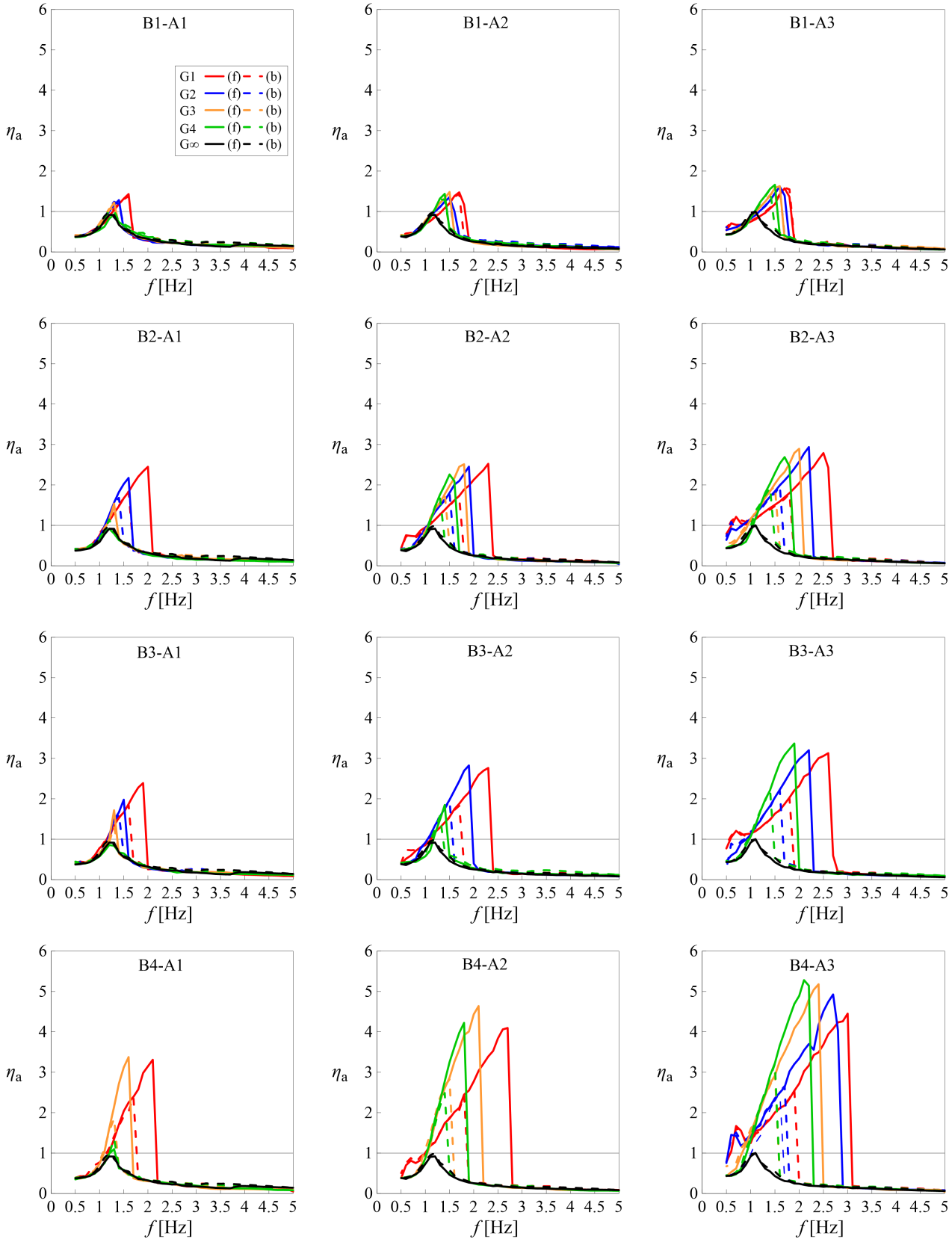


**Fig. 5** Experimental PRCs of $\eta_a$.

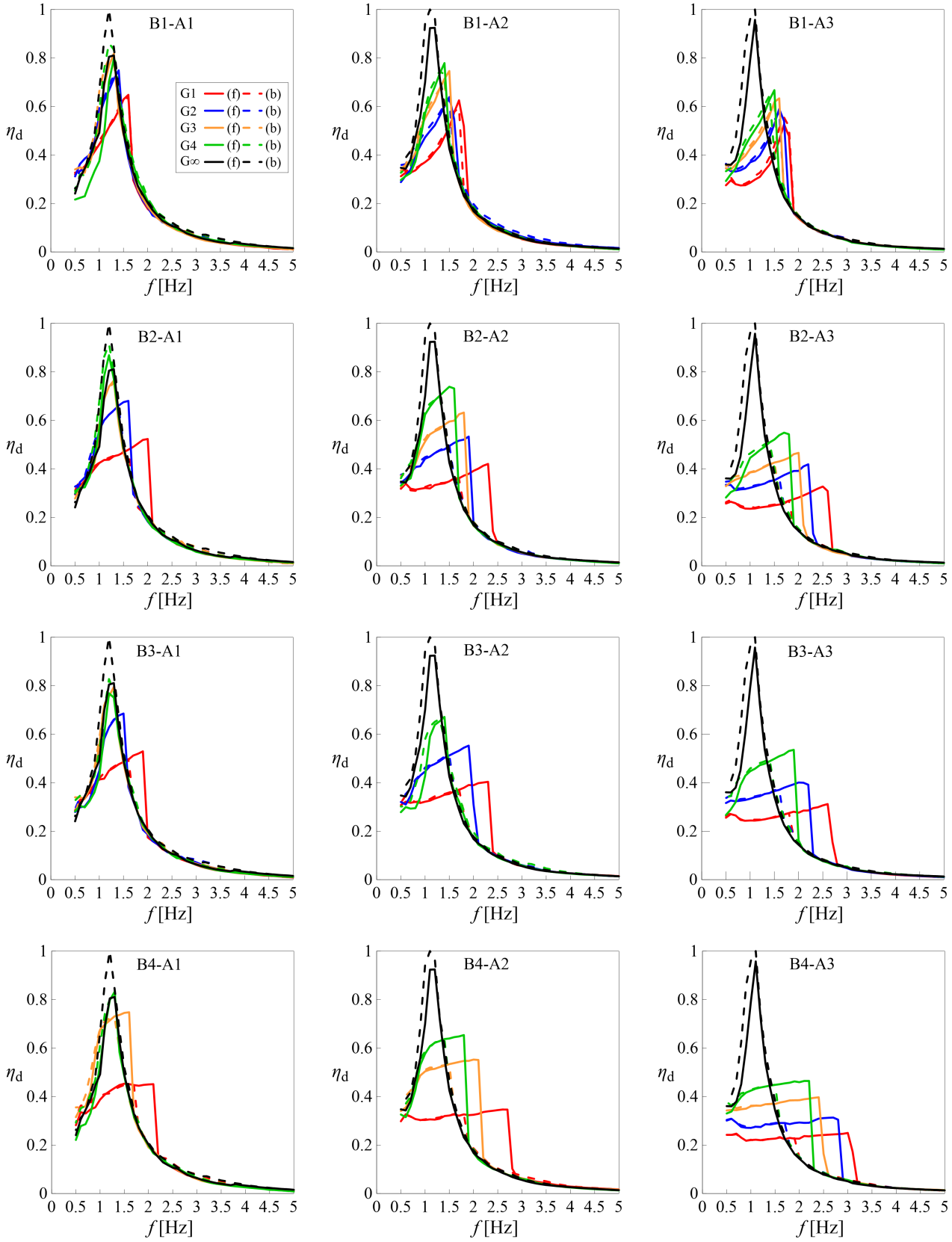


**Fig. 6** Experimental PRCs of $\eta_d$.

From Figure 6 it can be observed that, compared to the free flight condition, in presence of bumpers, due to the limitation of the displacement imposed by the constraint, $\eta_d$ is always lower than 1, both in the forward and in the backward sweeps, with the amplitude of the forward resonance greater then that of the backward resonance. This difference decreases increasing the stiffness of the bumper.

It can be observed that, in the absence of impact, PRCs overlap with those relating to the free flight condition. The overlap can occur on both the ascending branch, if impact occurs for frequencies greater that 0.5 Hz, and the descending branch, after the downward jump in the forward sweep and before the upward jump in the backward sweep. The upward jumps, compared to the PRCs of $\eta_a$ are less evident, especially in the case of large gaps and small accelerations.

As regards the variation of the jumps frequencies, and the appearance of secondary resonances, what has already been said for $\eta_a$ applies.

For a given pair B-A, which corresponds to a sub-figure in Figure 6 (for example B2-A2), compared to the free flight condition, as the total gap G decreases the maximum values of excursion, both in the forward and in the backward resonance condition decrease. In the ascending branch, the deviation from the PRCs associated with the free flight condition, occurs for gradually lower frequency values.

For a given pair B-G (see for example the second row of sub-figures, associated with the bumper B2 and focus the attention on the curves corresponding to the total gap G1), increasing the table acceleration, that is moving from the left column to the right column, it can be observed that the maximum values of excursion both in the forward and in the backward resonance condition decrease.

With the same acceleration A and total gap G (see for example the third column of sub-figures, associated with the acceleration A3 and focus the attention on the curves corresponding to the total gap G1), increasing the bumper stiffness, that is moving from the top to the bottom, it can be observed that the maximum values of excursion both in the forward and in the backward resonance condition decrease. It can also be observed that bumpers B2 and B3 behave in a similar way. Increasing B, with the same pair G-A, the penetration of the mass into the bumper decreases and becomes progressively independent of the forcing frequency. This branch, characterized by a concavity for the most deformable bumper, becomes gradually more straight and horizontal moving on to the bumper B4, which can be assimilated to a quite rigid obstacle.

As already emerged from the Figure 5, also from Figure 6, it can also be observed that in the case of the combination of the most deformable bumper with the smallest table acceleration (pair B1-A1, top left corner of the Figure) PRCs are quite similar to those associated with the free flight condition, while the difference becomes more evident for the pair characterized by the stiffest bumper and the greatest table acceleration (pair B4-A3, lower right corner of the Figure).

Finally, making a comparison, with the same frequency, between the PRCs with and without bumpers, it can be observed that in the presence of the bumpers there are frequency ranges in which, contrary to what one would expect, the excursion of relative displacement of the mass can be greater than what occurs in free flight condition.

Figures 5 and 6 provide analogous and dual indications, since they represent two different points of view from which to observe the same problem. In particular, they provide the same indications regarding the evolution of the jumps frequencies and the appearance of secondary resonances. Furthermore, they reflect the dual evolution of the represented quantities, namely accelerations and displacements, that is the introduction of the bumpers causes on the one hand the increase of the accelerations and on the other the decrease of the displacements.

### 4.3 Experimental scenarios

Based on the previous observations, as G decreases, different scenarios can be identified:

- Scenario 0 (S0): free flight condition;
- Scenario 1 (S1): grazing condition;
- Scenario 2 (S2): PRCs with only the primary resonance with right hysteresis;
- Scenario 3 (S3): PRCs with both the primary resonance with right hysteresis and the secondary resonance in the low frequency range.

In the following these scenarios will be described, starting from the scenario S3, in more detail. Phase portraits, Fourier spectra and time histories in steady-state condition will be analysed. In the time histories, the time axis $t$ will be normalized with respect to the period $T = 1/f$ of the harmonic base excitation.

*Scenario S3* PRCs belonging to this scenario show both the primary resonance with right hysteresis, between the downward and upward jumps, and a *secondary resonance without hysteresis* in the low frequency range without hysteresis. This scenario was experimentally obtained with different combinations of the investigated

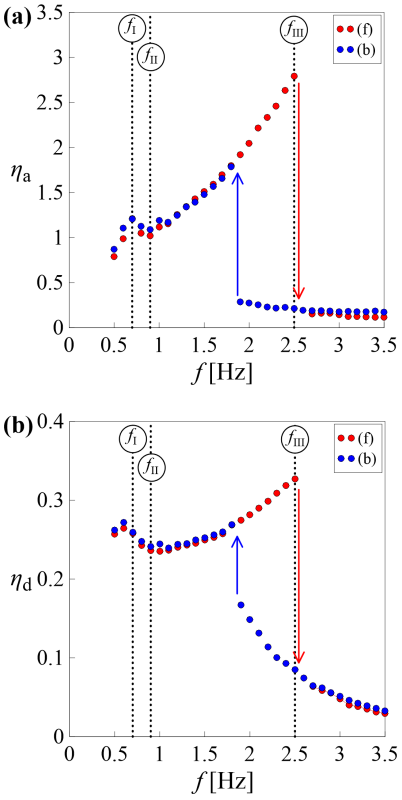


**Fig. 7** Scenario S3 (B2-G1-A3): a) $\eta_a$; b) $\eta_d$.

parameters. For example, the PRCs shown in Figure 7 correspond to the combination B2-G1-A3. The red markers refer to the forward sweep, while the blue ones to the backward sweep. The arrows indicate the two jumps. The three vertical dashed lines represent three values of frequency, corresponding respectively to the secondary resonance ($f_{\mathrm{I}}$ inside a circle), the following valley ($f_{\mathrm{II}}$ inside a circle) and the primary resonance ($f_{\mathrm{III}}$ inside a circle), that will be investigated in more detail. It is worth noting that, in this case impact occurs already at 0.5 Hz.

By focusing the attention on the ridge of the *secondary regular resonance without hysteresis* (first vertical dashed line on the left in Figure 7, denoted also with a $f_{\mathrm{I}}$ inside a circle), from Figure 8(a) it can be observed that, in the phase plane, the two solutions, corresponding to the forward (red line) and backward (blue line) sweep are approximatively coincident. The red and blue points represent the Poincaré sections and the two vertical dashed lines indicate the gaps. These two coincident solutions are characterized by several harmonic components (as can be seen from Figure 8(d)), whose amplitude decreases with increasing frequency. At the secondary resonance, in each forcing cycle the mass hits each bumper once, and these impacts are highlighted by peaks in the time history of the absolute acceleration (Figure 8(j)) and by sudden changes in relative velocity (Figure 8(m)). The time history of relative displacement is represented in Figure 8(g)) in which the horizontal dashed lines indicate the gaps. In the same Figures, two consecutive impacts, the first one with the right bumper and the second one with the left bumper, were highlighted with vertical yellow bands. The yellow points emphasize the instants of start and end of the contact phase and the corresponding values of displacement, acceleration and velocity, while the acceleration peaks are marked with cyan stars.

Moving to the next valley in the PRC (central vertical dashed line in Figure 7, denoted also with a $f_{\mathrm{II}}$ inside a circle), we still observe, in the phase plane, the presence of two coincident solutions (Figure 8(b)). As in the previous case, the two solutions are characterized by several harmonic components (Figure 8(e)) and, in each forcing cycle, the mass hits each bumper once (Figure 8(k)). In Figures 8(h), 8(k) and 8(n), two consecutive impacts, the first one with the right bumper and the second one with the left bumper, were highlighted with vertical yellow bands. In the same Figures, the yellow points emphasize the instants of start and end of the contact phase and the corresponding values of displacement, acceleration and velocity, while the acceleration peaks are marked with cyan stars.

Moving from the valley to the primary hysteresis, the solutions corresponding to the forward and backward sweeps are still coincident and, as the frequency increases, the phase portraits gradually regularize and take on the appearance of an ellipse.

By focusing the attention on the primary resonance with right hysteresis (third vertical dashed line in Figure 7, denoted also with a $f_{\mathrm{III}}$ inside a circle), just before the downward jump, from Figure 8(c) it can be observed that, in the phase plane, there are two different steady-state solutions:

- Large-amplitude resonant motion associated with the occurrence of impact (red line);
- Small-amplitude non-resonant motion without impact (blue line).

The two solutions are both periodic with one predominant harmonic component (Figure 8(f)). Actually, there would be also an unstable solution, that could not be obtained experimentally. By focusing the attention on the large-amplitude motion, it can be observed that, in each forcing cycle, the mass hits each bumper once. In Figures 8(i), 8(l) and 8(o), two consecutive impacts, the first one with the right bumper and the second one with the left bumper, were highlighted with vertical yellow bands. In the same Figures, the yellow points emphasize the instants of start and end of the contact phase and

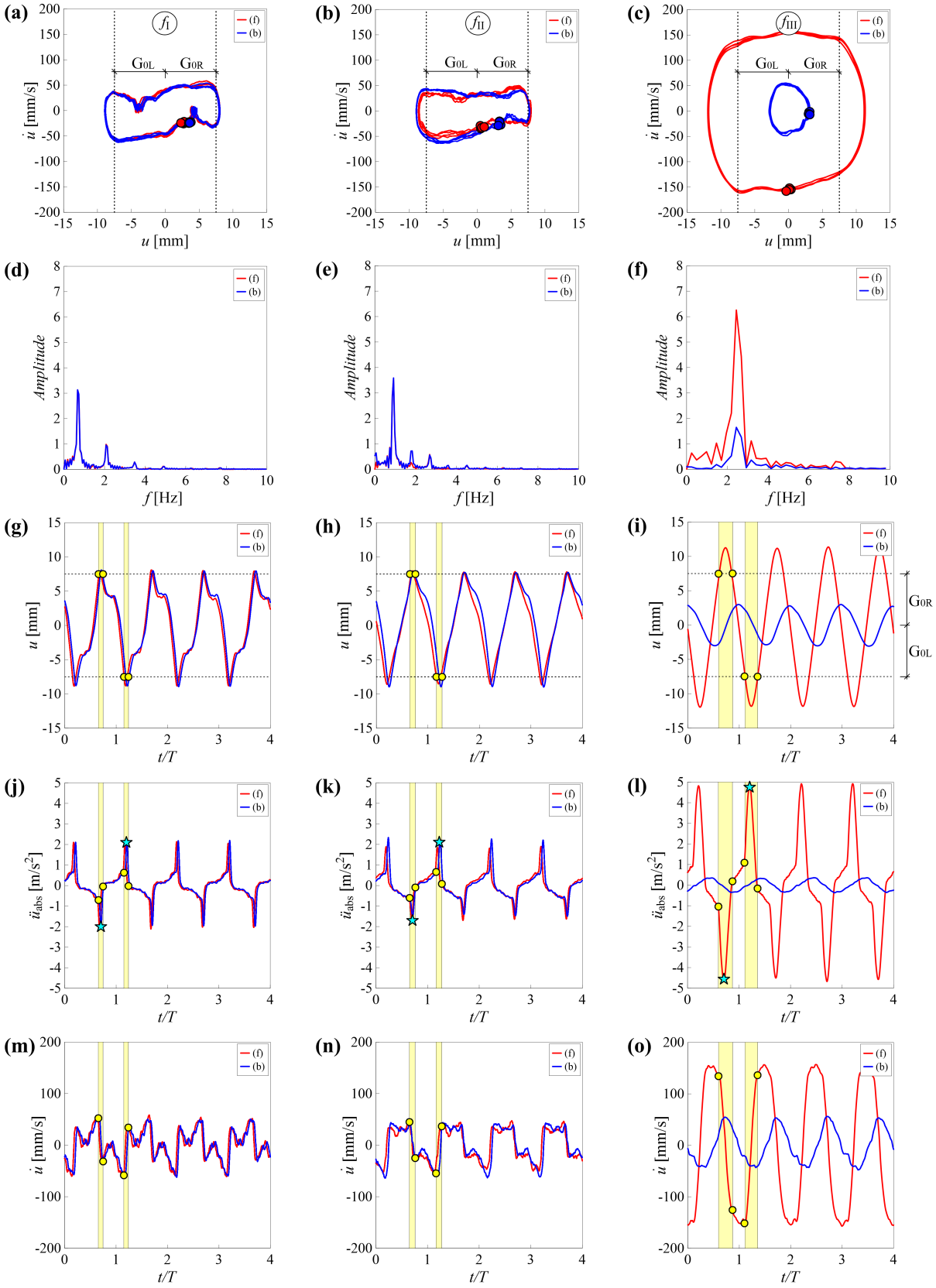


**Fig. 8** Scenario S3 (B2-G1-A3): Phase portrait: a) $f = f_{\mathrm{I}}$; b) $f = f_{\mathrm{II}}$; c) $f = f_{\mathrm{III}}$; Fourier spectrum: d) $f = f_{\mathrm{I}}$; e) $f = f_{\mathrm{II}}$; f) $f = f_{\mathrm{III}}$; Time history of relative displacement: g) $f = f_{\mathrm{I}}$; h) $f = f_{\mathrm{II}}$; i) $f = f_{\mathrm{III}}$; Time history of absolute acceleration: j) $f = f_{\mathrm{I}}$; k) $f = f_{\mathrm{II}}$; l) $f = f_{\mathrm{III}}$; Time history of relative velocity: m) $f = f_{\mathrm{I}}$; n) $f = f_{\mathrm{II}}$; o) $f = f_{\mathrm{III}}$.

the corresponding values of displacement, acceleration and velocity, while the acceleration peaks are marked with cyan stars.

Immediately after the downward jump, for greater values of frequency, there is only one solution, the same in the forward and in the backward sweep, characterized by the absence of impact and the corresponding phase portrait takes on the appearance of an ellipse.

It is worth noting that the considered setup (B2-G1-A3) is characterized by an accidental geometric dissymmetry, which is reflected in the asymmetry of the phase portraits and of the time histories. This dissymmetry is due to imperfections in the experimental setup, related to the gap, which is not perfectly symmetrical and slightly different from the nominal value. This is particularly evident in Figures 8(a) and 8(b) and less visible in Figure 8(c), given the greater penetration of the mass into the bumpers. Furthermore, from Figure 8, it can be observed that the duration of the contact time compared to the period $T = 1/f$ of the harmonic base excitation (width of a single vertical yellow band), increases going from $f = f_{\mathrm{I}}$ to $f = f_{\mathrm{III}}$.

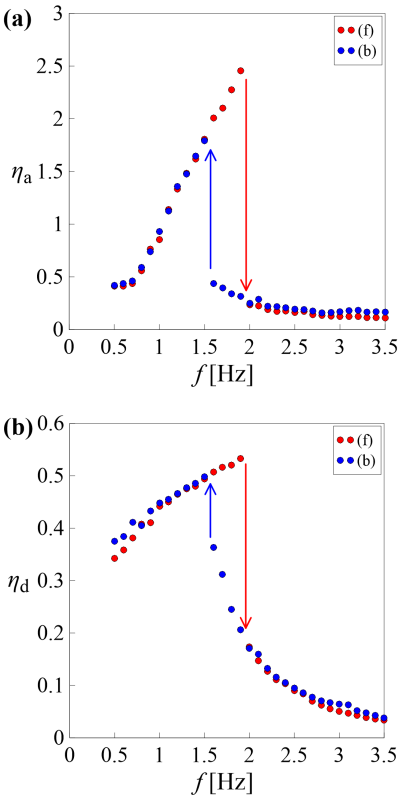


**Fig. 9** Scenario S2 (B2-G2-A2): a) $\eta_a$; b) $\eta_d$.

*Scenario S2* PRCs belonging to this scenario are characterized only by the presence of the primary resonance with right hysteresis, between the downward and upward jumps. This scenario was experimentally obtained with different combinations of the investigated parameters. For example, the PRCs shown in Figure 9 correspond to the combination B2-G2-A2. In the frequency range between the two jumps, everything goes as described above. Unlike the case examined in the previous paragraph (scenario S3), here, having increased the gap, impact does not occur immediately starting from the smallest frequency value investigated, but in the range between 0.7 and 2 Hz.

*Scenarios S1* In the grazing condition, the mass just touches the bumpers without deforming them significantly. Consequently, the corresponding PRCs are similar to those occurring in the free flight condition. The grazing condition was experimentally observed in few cases where the combination of the largest gap and the smallest excitation amplitude occurred (Figure 10, corresponding to the combination B2-G4-A1).

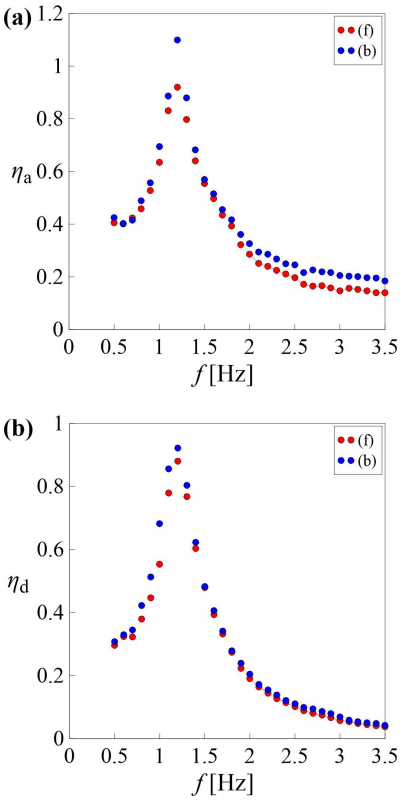


**Fig. 10** Scenario S1 (B2-G4-A1): a) $\eta_a$; b) $\eta_d$.

*Scenarios S0* As concerns the free flight condition, what has already been said in Subsection 4.1 applies.

## 5 Identification via the Simplified Nonlinear Model (SNM)

The experimental results were compared with those obtained with a numerical model, as described in Section 2, in which a linearization of the behaviors of both the bumpers and the damper was made, retaining the other nonlinearities. In particular, the behavior of both damper and bumpers was modelled with a linear elastic spring in parallel with a linear viscous dashpot. Consequently, the restoring forces in Equations 1, 2 and 3 assume the expression:

$$F(t) = Ku(t) \tag{5a}$$

$$F_{\mathrm{j}}(t) = K_{\mathrm{j}} u_{\mathrm{j}}(t) \quad (\mathrm{j} = \mathrm{R,L}) \tag{5b}$$

where $K$ and $K_{\mathrm{j}}$ (j = R, L) are the elastic stiffness of the damper and the bumpers respectively. In the case of two equal bumpers symmetrically positioned on the two sides of the mass, it is $K_{\mathrm{R}} = K_{\mathrm{L}}$. By virtue of the linearization made, this model was called Simplified Nonlinear Model (SNM). It is worth noting that the other sources of nonlinearities, namely the gap, the unilateral constrains and the impact that induces abrupt changes of both stiffness and damping, are taken into account.

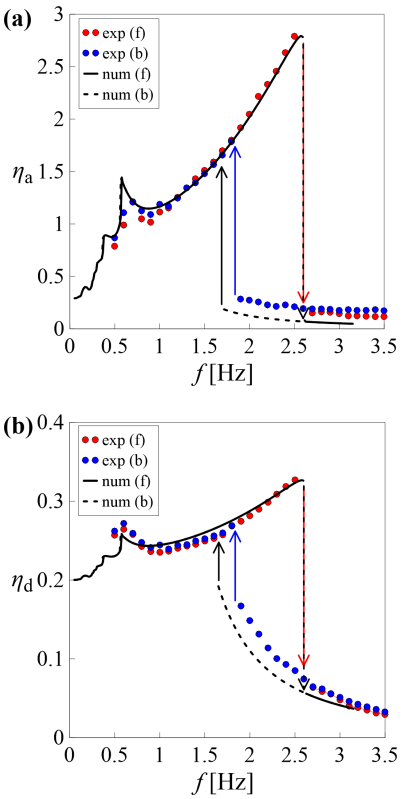


**Fig. 11** Comparison between experimental and numerical PRCs (Scenario S3, combination B2-G1-A3): a) $\eta_a$; b) $\eta_d$.

The authors are aware of the limitations of the linear visco-elastic model, particularly when used to model the contact; however, they consider this model satisfactory for their purposes. To compare the experimental results with those obtained with the SNM, it was necessary to reduce the nonlinear constitutive law of the damper [54,61] to a linear elastic one. This was made considering an equivalent stiffness $K$, estimated in free flight resonance condition, for each value of table acceleration A.

Once the parameters of the numerical model were identified, the scenarios described above were reproduced numerically and a comparison with the experimental data was made in terms of PRCs and phase portraits, as shown in Figures 11, 12 and 13. In particular, Figures 11 and 12 show the PRCs and the phase portraits corresponding to the S3 scenario for the B2-G1-A3 combination; and Figure 13 shows the PRCs of the S2 scenario for the B2-G2-A2 combination. In these Figures, the experimental results were represented with markers in the PRCs (Figures 11 and 13) and dotted lines in the phase portraits (Figure 12), while the numerical results were represented with solid and dashed black lines. The identified parameters of the model were: $K_{\mathrm{R}} = K_{\mathrm{L}} = 510$ kN/m, $C_{\mathrm{R}} = C_{\mathrm{L}} = 0.9$ kN s/m for the bumper B2 and, with regards to the damper, $K = 26.8$ kN/m, $C = 1.1$ kN s/m for the scenario S3 and $K = 31.9$ kN/m, $C = 1.1$ kN s/m for the scenario S2.

It can be observed that, although the SNM does not include the nonlinearities associated with the behavior of both the damper and the bumpers, there is a good agreement between experimental and numerical results both in terms of PRCs (Figures 11 and 13) and in the phase portraits (Figure 12). The model is able to reproduce both qualitatively and quantitatively the primary resonance and the downward jump, whereas it is not able to precisely capture other phenomena such as the frequency of the upward jump. This is due to the difference between the experimental (nonlinear) and numerical (linear) PRCs in free flight condition which causes that, for a given value of the gap, in the SNM, the upward jump occurs for lower values of the frequency. Furthermore, the position and amplitude of the secondary resonance was reproduced in a sufficiently accurate manner. The numerical model also highlighted the presence of internal loops in the phase portrait, corresponding to the secondary resonance ($f = f_{\mathrm{I}}$, black cycle in Figure 12(a)) and something similar to small loops can also be recognized in the experimental cycles.

Based on these considerations, the SNM appears to be adequate to simulate the behavior of the system and

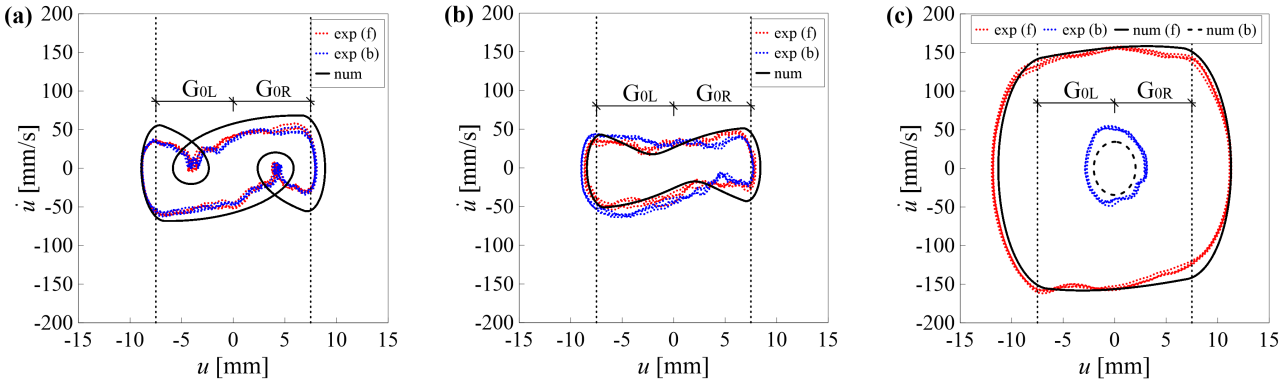


**Fig. 12** Comparison between experimental and numerical phase portraits (Scenario S3, combination B2-G1-A3): a) $f = f_{\mathrm{I}}$; b) $f = f_{\mathrm{II}}$; c) $f = f_{\mathrm{III}}$.

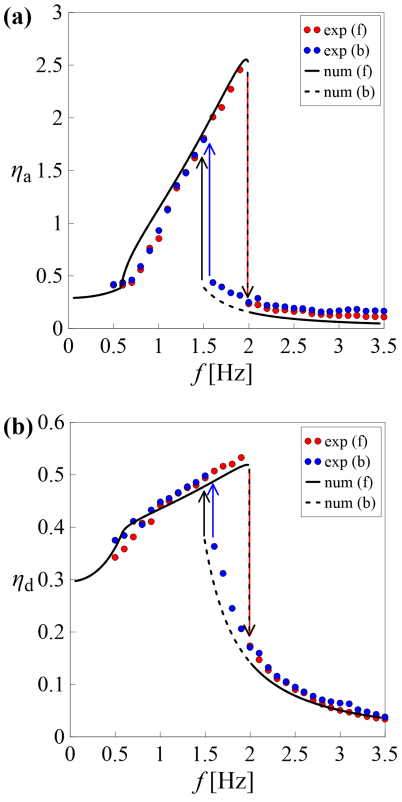


**Fig. 13** Comparison between experimental and numerical PRCs (Scenario S2, combination B2-G2-A2): a) $\eta_a$; b) $\eta_d$.

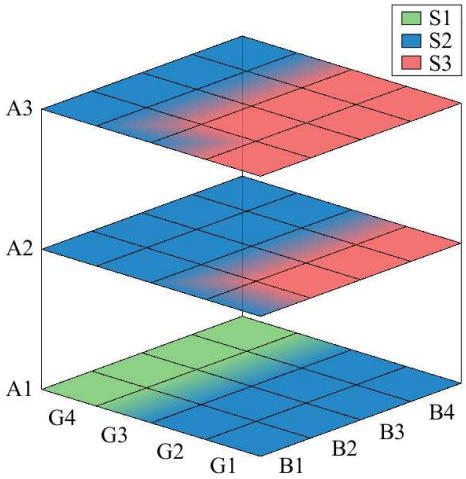


**Fig. 14** Investigated cases and scenarios.

can give quite satisfying results in good agreement with the experimental outcomes.

## 6 Further numerical scenarios

From the analysis of the experimental results, it was observed that the scenarios become more and more complex decreasing the total gap G, increasing the peak table acceleration A and the bumper's stiffness B (Figure 14). In this Figure, each plane corresponds to a value of peak table acceleration A, which grows moving from the lower to the higher plane. In each plane, every single square of the grid correspond to a pair B-G and the corresponding color denotes the associated scenario (S1: green, S2: blue, S3: red). It can be observed that, for the lower value of A (A1), only the scenarios S1 and S2 were observed, the former only for the pair G4-A1; for values of G greater than G4, free flight condition occurs. Increasing A, only the scenarios S2 and S3 were observed and the transition from S2 to S3 occurs decreasing the total gap G and increasing the stiffness of the bumper B; furthermore, the extension of the red region, associated with the scenario S3, increases. The grazing condition was not observed for these values of A, i.e. A2 and A3, because it occurs for values of G$\infty$ greater than G4.

Based on these considerations, using the SNM, which has proven to be able to reproduce satisfactorily the experimental results, further numerical simulations were carried out to investigate what happens for combina-

tions of the parameters not accomplished in the experimental tests.

Having available for the moment the same bumpers Bk (k = 1, 2, 3, 4) used in the experimental campaign, new combinations can be obtained varying the gap amplitude G and the peak table acceleration A. In order to investigate the existence of more complex scenarios, one choice may be to keep the peak table acceleration A fixed and to reduce the total gap G.

In Figure 15 the numerical PRCs corresponding to the combination B3-A3 with a total gap amplitude G = 10 mm are represented. It can be observed that, compared to the previously defined scenario S3, in this case in the low frequency range different types of secondary resonances arise. In particular, for $f < 0.9$Hz, several *secondary resonances with left hysteresis* are observed (see the area enclosed by a dotted grey circle). On the other hand, in the neighbourhood of 1 Hz (rectangular zoomed area), a *secondary non-regular resonance without hysteresis*, is noticed .

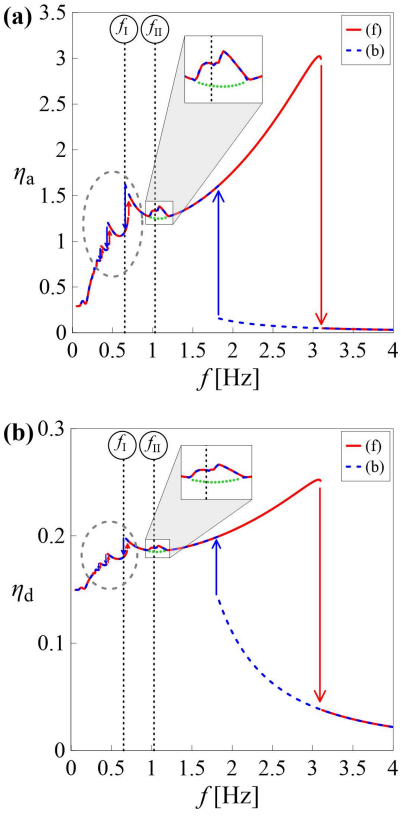


**Fig. 15** Numerical PRCs (B3-A3, G = 10 mm): a) $\eta_a$; b) $\eta_d$.

By focusing the attention on one of the *secondary resonances with left hysteresis* (first vertical dashed line on the left in Figure 15, denoted also with a $f_I$ inside a

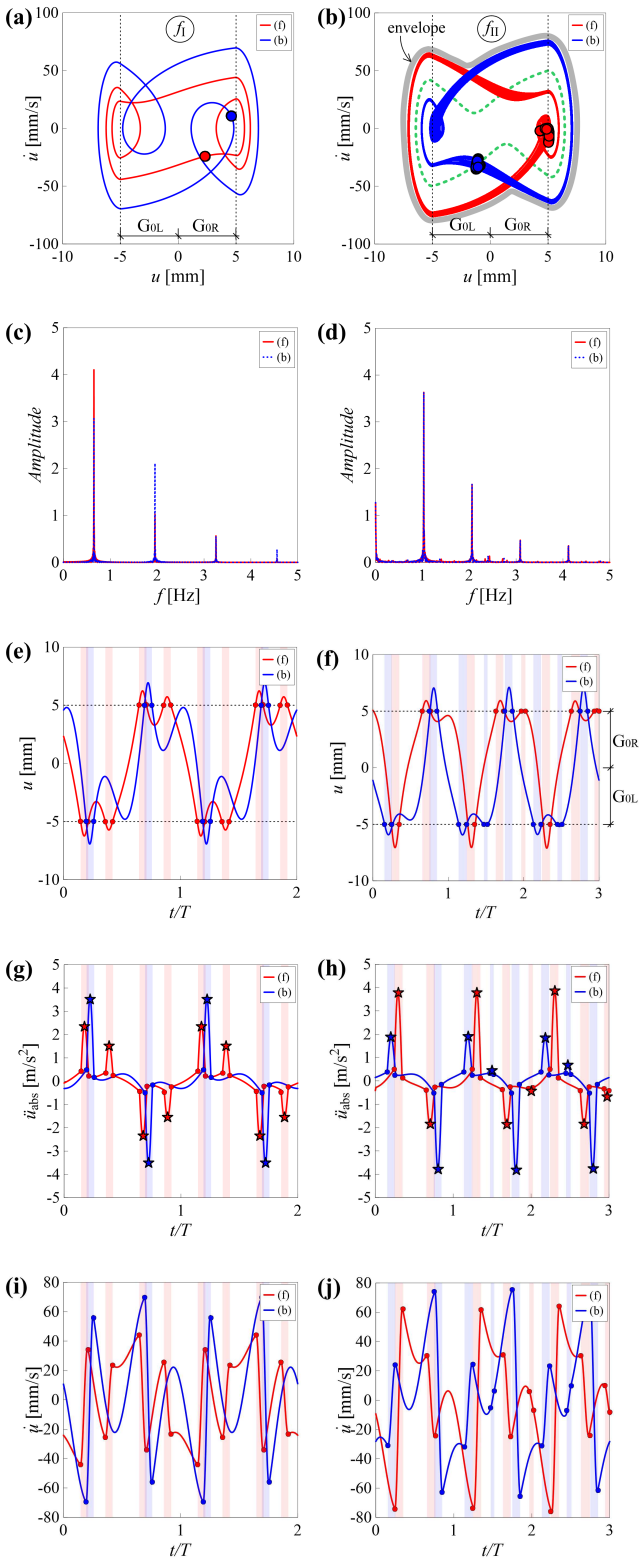


**Fig. 16** Numerical results (B3-A3, G = 10 mm). Phase portrait: a) $f = f_I$; b) $f = f_{II}$; Fourier spectrum: c) $f = f_I$; d) $f = f_{II}$; Time history of relative displacement: e) $f = f_I$; f) $f = f_{II}$; Time history of absolute acceleration: g) $f = f_I$; h) $f = f_{II}$; Time history of relative velocity: i) $f = f_I$; j) $f = f_{II}$.

circle), it can be observed that, there are two different steady-state solutions (Figure 16(a)):

- Large-amplitude motion with impact (blue line);
- Small-amplitude motion with impact (red line).

Each of the two limit cycles in Figure 16(a) is antisymmetric with respect to the axes. Compared to the primary resonance (see Figure 8(c)), here the large-amplitude motion is associated with the backward sweep. Furthermore, the two solutions are both periodic multi-frequency (Figure 16(c)) and are characterized by the occurrence of impact, as it can be seen also from Figures 16(e), 16(g), 16(i). In particular, in each forcing cycle, the mass hits each bumper twice in the forward sweep (vertical light red bands) and once in the backward sweep (vertical light blue bands). The corresponding acceleration peaks are marked with red (forward sweep) and blue (backward sweep) stars respectively. The number of impacts can also be deduced from the phase portraits (Figure 16(a)). Both the limit cycles are characterized by the presence of internal loops. In the backward sweep, these loop do not touch the vertical dashed lines that represent the position of the obstacles, whereas in the forward sweep, the loop cross them. As in the primary hysteresis, also here there would be also an unstable solution, that could not be obtained experimentally.

Similar considerations apply to the other *secondary resonances with left hysteresis* that occur for smaller frequency values. What changes, in addition to the amplitude of the response, is the number and the position of the internal loops in the phase portraits and, thus, the number of impacts. In particular, decreasing the frequency, the number of impacts per forcing cycle increases, both in the forward and in the backward sweep, with a greater number of impacts always on the forward sweep.

As concerns the *secondary non-regular resonance without hysteresis* (second vertical dashed line in Figure 15, denoted also with a $f_{\mathrm{II}}$ inside a circle), it can be observed that, in this frequency range, forward and backward PRCs overlap, therefore there is no hysteresis. In the central part of this resonance, characterized by a more or less constant excursion of both absolute acceleration and relative displacement, a *pair of quasi-periodic solutions* is observed (Figures 16(b) and 16(d)). These two limit cycles have the same excursion but are characterized by an eccentricity, calculated as the half-sum of maximum and minimum values at steady state of each sub-frequency range, equal in absolute value but with opposite sign. Consequently, the two solutions are not antisymmetric in themselves, but the antisymmetry is achieved through their envelope, as can be seen from Figure 16(b), in which the envelope is highlighted in light grey. Each cycle has an internal loop which, as time goes by, approaches, crosses and then moves away from one of the left vertical dashed lines representing the position of the obstacles. In particular, the internal loop of the red cycle crosses only the right vertical line (right bumper), while the internal loop of the blue cycle crosses only the left vertical line (left bumper). Given the quasi-periodicity of the response, it is not possible to reach a steady-state condition. This results, for each of the two solutions that make up the pair, in a different number of impacts, in each forcing cycle, to the right and left as time goes on (Figures 16(f), 16(h), 16(j)). In this frequency range, starting from appropriate initial conditions, it is possible to observe, besides the pair of quasi-periodic solutions, also a periodic solution, represented with a dashed green curve in Figure 16(b). Compared to the two quasi-periodic solutions, this solution is antisymmetric in itself and is characterized by a smaller excursion and zero eccentricity. In the PRCs (Figure 15) the values of excursion associated with these periodic solutions are placed on the dashed green curve, which represents the ideal course of the PRC that would have occurred in the absence of the secondary non-regular resonance.

After passing the range characterized by almost constant excursion, along the subsequent descending branch, the presence of a pair of solutions, with an antisymmetric envelope, is still observed and both the quasi-periodicity and the internal loops gradually disappear increasing the frequency. In the next ascending branch, before the primary hysteresis, we return to having a single periodic solution.

In Figure 17 the numerical PRCs corresponding to the combination B3-A3 with the bumpers initially attached to the mass (G = 0 mm) are represented. It can be observed that the situation returns to be smooth, the forward and backward curves overlap without jumps, hysteresis or secondary resonances and the primary resonance has moved to higher frequencies (about 5.4 Hz).

For each frequency value, there is always a single periodic mono-frequency solution (Figures 18(a) and 18(b), the same on both the forward and backward sweep, and the mass, during its motion, would seem to be always in a contact condition, alternatively with a bumper or the other (Figures 18(c), 18(d) and 18(e)). In reality, there is also in this case a phase of free flight but it is very short. This is related to the small value of the relaxation time of the bumper, which causes the detachment between the mass and the bumper to take place when the latter has recovered practically all its deformation and immediately afterwards the mass impacts the other bumper, which in the meantime has already recovered its deformation. This can be seen better by

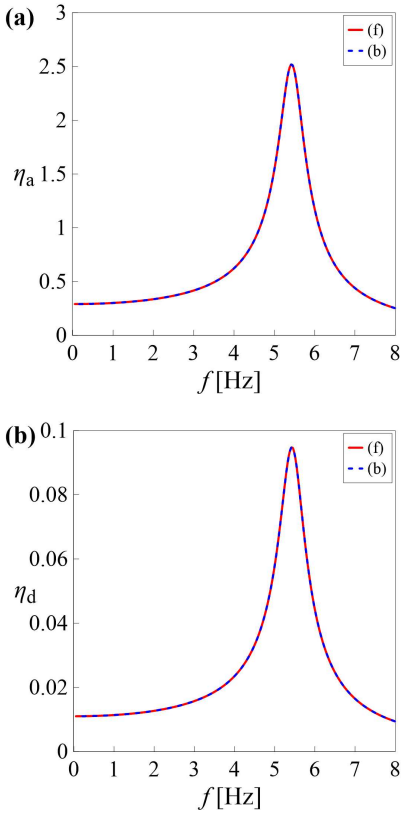


**Fig. 17** Numerical PRCs (B3-A3, G = 0 mm): a) $\eta_a$; b) $\eta_d$.

looking at the zoomed areas in Figure 18(c), in which, in addition to the relative displacement of the mass, also the clearance functions $G_{\mathrm{R}}(t)$ (green curve) and $G_{\mathrm{L}}(t)$ (orange curve) are represented. Focusing on the zoomed area at the top of the Figure, it can be observed that, after the detachment between the mass and the right bumper, highlighted with a green dot, the right bumper recovers its deformation (green curve) while the mass goes towards the left bumper and the subsequent contact is highlighted with an orange dot.

Repeating the numerical analysis, conducted for the pair B3-A3, for other values of the total gap G and representing all the corresponding PRCs in the same graph, Figure 19 is obtained. The two sub-figures are the numerical equivalent of the experimental ones (see the sub-figures of Figures 5 and 6 corresponding to the pair B3-A3), in which the range of investigated gap values has been expanded. Consequently, using the SNM it was possible to integrate the experimental results and fill the void left by experimentation in order to have a more complete description of the PRCs evolution with the total gap G.

In Figure 19, solid line represent the forward sweep, dashed lines the backward sweep, the vertical arrows indicate the two jumps and each color corresponds to a scenario. Compared to the scenarios observed exper-

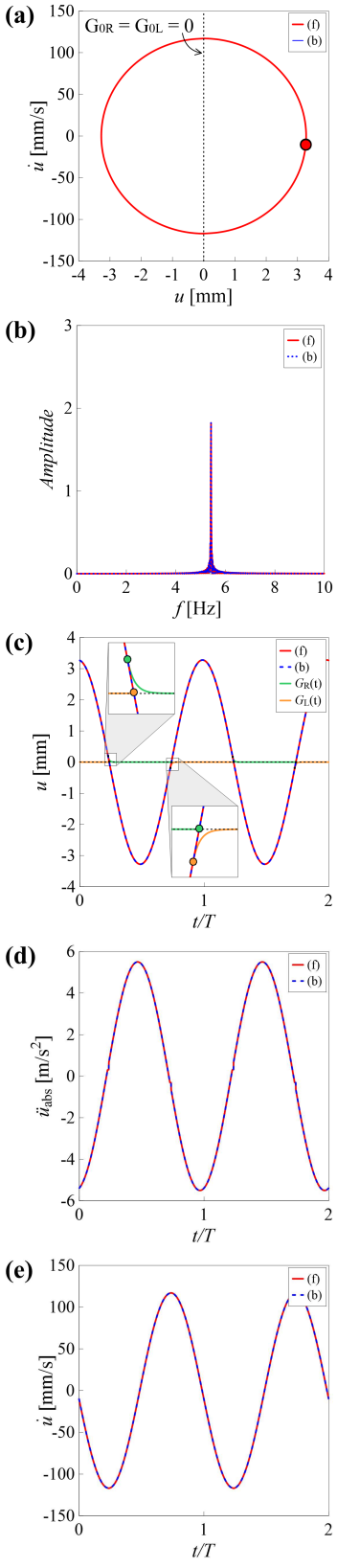


**Fig. 18** Numerical results (B3-A3, G = 0 mm), resonance condition: a) Phase portrait; b) Fourier spectrum; c) Time history of relative displacement; d) Time history of absolute acceleration; e) Time history of relative velocity.

imentally and represented respectively with the colors green (S0 and S1), blue (S2) and red (S3), magenta was used to highlight the PRCs similar to those shown in Figure 15 (the corresponding scenario will be denoted as scenario S4) and light blue for the PRCs (similar to those shown in Figure 17) corresponding to a zero initial gap (the corresponding scenario will be denoted as scenario S5). It is worth noting that, using the Simplified Nonlinear Model (SNM), PRCs corresponding to the grazing condition (scenario S1) coincide with those relating to free flight (scenario S0), which are the typical dynamic amplification curves of a visco-elastic system, without jumps and softening. From Figure 19, it can be observed that, the trends experimentally observed (see Subsection 4.2) found confirmation in the numerical results.

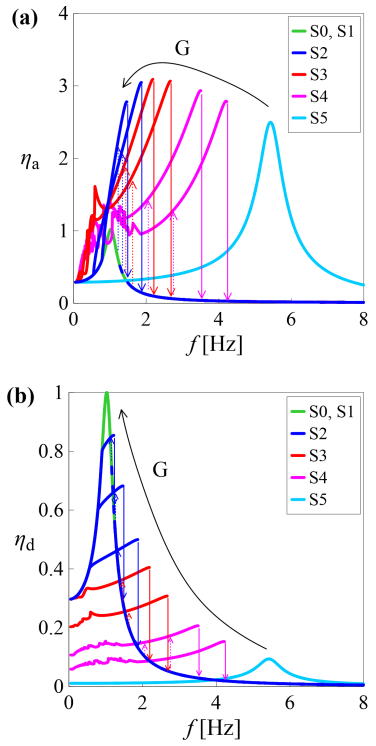


**Fig. 19** Numerical PRCs for the pair B3-A3 and different values of the total gap G: a) $\eta_a$; b) $\eta_d$.

In Figure 20 numerical PRCs corresponding to the pair G3-A1 and increasing values of bumper's stiffness B are represented in the same graph. It can be observed that, for the selected pair G-A, secondary resonances do not occur even for high values of bumper's stiffness. Most of the PRCs belong to the scenario S2 (color blue), except for very small values of stiffness. In these cases (in the following denoted as scenario S6), forward and backward PRCs (in Figure 20 represented with orange curves) are slightly bent to the right and overlap without jumps and hysteresis; in the frequency range associated with the occurrence of the impact, a single periodic mono-frequency solution is observed. The green PRCs correspond to the free flight condition (absence of bumpers). Also in this case, the trends experimentally observed (see Subsection 4.2) found confirmation in the numerical results.

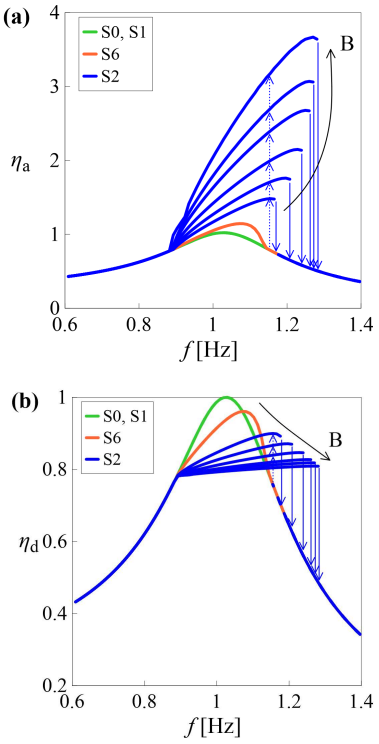


**Fig. 20** Numerical PRCs for the pair G3-A1 and different values of the bumper's stiffness B: a) $\eta_a$; b) $\eta_d$.

Based on the numerical results obtained with the SNM which, despite its relative simplicity, has proven to be able to reproduce the experimental scenarios satisfactorily, one of the future developments of this study will be to understand if the further numerical scenarios can be obtained also experimentally.

## 7 Interpretation of the results in terms of dimensionless parameters

The SDOF system response can be described also in terms of the following dimensionless parameters:

- $\lambda_j = K_j/K$ (j = R, L): ratio between the stiffness of the $j$-th bumper and that of the damper;
- $\tau_{rj} = \omega C_j/K_j$ (j = R, L): dimensionless relaxation time of the $j$-th bumper;
- $\delta_{0j} = G_{0j}/u_{max}$ (j = R, L): dimensionless initial gap, that is the initial distance between the mass

**Table 1** Dimensionless parameters

| | $\delta$ | | | | | $\lambda$ | | | |
|---|---|---|---|---|---|---|---|---|---|
| | G1 | G2 | G3 | G4 | G$\infty$ | B1 | B2 | B3 | B4 |
| A1 | 0.47 | 0.62 | 0.78 | 0.93 | $\geq 1.00$ | 2.9 | 15.0 | 20.0 | 67.8 |
| A2 | 0.30 | 0.40 | 0.49 | 0.59 | $\geq 1.00$ | 3.5 | 17.8 | 23.7 | 80.1 |
| A3 | 0.22 | 0.29 | 0.36 | 0.43 | $\geq 1.00$ | 3.8 | 19.4 | 25.9 | 87.5 |

and the $j$-th bumper normalized with respect to the maximum displacement of the SDOF system (mass M and damper D, Figure 1) in the free flight resonance condition. Based on this normalization, a value $\delta_{0j} = 0$ indicates that the $j$-th bumper is initially attached to the mass; if $\delta_{0j}$ takes values between 0 and 1, the mass beats and deforms the $j$-th bumper; a value $\delta_{0j} = 1$ indicates that the mass can only graze the $j$-th bumper without deforming it; whereas the mass will be in the free flight condition for $\delta_{0j} > 1$;

– $\xi$: damping factor of the SDOF system.

For symmetrically positioned equal bumpers it is $\lambda_R = \lambda_L = \lambda$, $\tau_{rR} = \tau_{rL} = \tau_r$ and $\delta_{0R} = \delta_{0L}$. Consistently with what has been done in physical terms, in the following the dimensionless total gap, defined as the sum of $\delta_{0R}$ and $\delta_{0L}$, was denoted simply with $\delta$, without subscript.

The estimation of the values of the dimensionless parameters, corresponding to each experimentally investigated combination of bumper stiffness B, total gap amplitude G and peak table acceleration A, was made assuming a constant value of the damping factor $\xi$ equal to 0.15.

In the numerical investigations carried out using the SNM, we considered, for each value of peak table acceleration A, an equivalent stiffness $K$ of the damper, evaluated in free flight resonance condition. Consequently, to each bumper B correspond three values of $\lambda$, increasing with A (Table 1). For the same peak table acceleration A, $\lambda$ increases with the stiffness of the bumper B. It can be observed that $\lambda$, so esteemed, in our case is always greater than 1 and takes on values between about 3 (combination of the most deformable bumper with the smallest table acceleration) and about 90 (combination of the stiffest bumper with the greatest table acceleration). Furthermore, for the types of bumpers considered in the experimental laboratory campaign the relaxation time $\tau_r$ does not vary significantly and consequently it was assumed constant and equal to 0.01.

As concerns the dimensionless gap $\delta$, since the maximum displacement of the SDOF system $u_{max}$ depends on the peak table acceleration A, twelve values of $\delta$ were considered, each one corresponding to a combination of A and G (Table 1). The dimensionless total gap

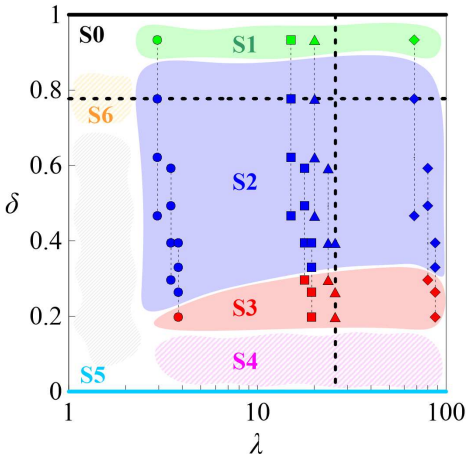


**Fig. 21** Investigated cases in terms of dimensionless parameters ($\xi = 0.15$, $\tau_r = 0.01$).

increases with the total gap amplitude G, for a given value of A, and decreases increasing A, for a given value of G. It can be observed that $\delta$ in our case takes on values greater than 0.22.

In Figure 21 the cases investigated experimentally are represented in terms of dimensionless parameters in the $\lambda - \delta$ plane for fixed values of $\xi$ and $\tau_r$. As in Figure 14, each color corresponds to a scenario; in addition to the scenarios experimentally observed (S0: black horizontal line $\delta = 1$ and vertical line $\lambda = 0$, the latter not shown, S1: green region, S2: blue region, S3: red region), also those highlighted by the numerical model (S4: magenta region, S5: light blue horizontal line $\delta = 0$, S6: orange region) are represented. Each symbol corresponds to a bumper (B1: circle, B2: square, B3: triangle, B4: diamond). To each bumper correspond three values of stiffness ratio $\lambda$ (three vertical dashed lines), one for each value of table acceleration A. For each value of $\lambda$ (combination B-A) there are four values of $\delta$, one for each value of total gap G.

Figure 21 can be seen as the translation in dimensionless terms of Figure 14. The transition to the dimensionless parameters therefore allowed to synthesize in a single graph the results of both the experimental and numerical investigations. It is worth noting that, while in physical terms the gap corresponding to grazing G$\infty$ depends on the table acceleration, in dimen-

sionless terms this condition translates into a single value $\delta = 1$.

It can be noted that the values of $\lambda$ associated with the two bumpers B2 and B3 are close to each other. This is due to the fact that these two bumpers have similar stiffness. It can be observed that most of the experimental tests are associated with the scenario S2 (intermediate values of $\delta$), four tests (highest values of $\delta$) can be associated with the scenario S1 and the remainder with the scenario S3 (smallest values of $\delta$). The experimental investigation did not cover a portion of the $\lambda-\delta$ plane. In particular, the vertical band characterized by $\lambda < 2$ and the horizontal band characterized by $\delta < 0.2$ were not explored. Some indications on the scenarios that could arise in these regions have been provided by the SNM (scenarios S4, S5, S6), which has proven to be able to reproduce the experimental results satisfactorily. The unexplored area (light grey shaded area) will be investigated with more detail in future developments of this work, because it is not said that, for example, within the magenta region (scenario S4), there is only the behavior shown in Figure 15.

Once the dimensionless parameters were introduced, Figures 5 and 6, represented and described in Subsection 4.2 in terms of physical parameters (B, G, A), can be reread also in terms of dimensionless parameters. In particular, each graph of Figures 5 and 6, associated with a pair B-A, corresponds to a specific value of $\lambda_{\mathrm{ki}}$ (the subscript $k$ is associated with the bumper Bk, k = 1, 2, 3, 4 and the subscript $i$ is associated with the acceleration Ai, i = 1, 2, 3) and each curve of the graph corresponds to a specific value of dimensionless gap $\delta_{\mathrm{ji}}$ (the subscript $j$ is associated with the total gap Gj, j = 1, 2, 3, 4 and the subscript $i$ is associated with the acceleration Ai, i = 1, 2, 3). Thus, each sub-figure of Figures 5 and 6 corresponds to a section $\lambda = constant$ in Figure 21. Figure 19 coincides with one of these section, and it was highlighted with a vertical dashed black line $\lambda = 25.9$. Along each section $\lambda = constant$, if A is kept fixed and G is reduced, this means reducing $\delta$ and thus moving downward. Also Figure 20 can be synthetically represented in Figure 21. It corresponds to the section $\delta = 0.78$, highlighted with an horizontal dashed black line. In fact, each section $\delta = constant$ corresponds to a specific pair G-A along which to increase B means increase $\lambda$ and therefore move to the right.

The introduction of dimensionless parameters hallowed to generalize the obtained results, to reduce the number of parameters that influence the response of the system and to highlight how what matters are, not the values assumed by the individual physical parameters, but rather their relationships. This causes that the same result can be obtained with different combinations of the involved physical parameters.

## 8 Conclusions and future developments

In this paper, some of the scenarios which can occur in the experimental nonlinear nonsmooth response of a vibro-impact SDOF system, symmetrically constrained by deformable and dissipative bumpers under harmonic excitation (forward and backward sine sweep signal), were identified and described. The scenarios were classified by observing the characteristics of forward and backward Pseudo Resonance Curves (PRCs) of normalized excursion of absolute acceleration and relative displacement, obtained varying selected parameters, namely peak table acceleration A, amplitude of the total gap G and bumper's stiffness B.

In free flight condition, that is in the absence of bumpers, the softening behavior of the damper causes the PRCs to be bent to the left, with a resonance frequency gradually decreasing as the table acceleration increases, whereas the amplitude of the response increases. Compared to this reference situation, in the presence of the bumpers, the hardening caused by the occurrence of impact bend the PRCs to the right, with the consequent appearance of jumps and hysteresis. Furthermore, the presence of the bumpers produces, compared to the free flight condition, on the one hand an increase in acceleration and, in a dual manner, a decrease in displacement.

It was observed that, the variation of the investigated parameters (A, G, B) influences the PRCs. In particular, the jump frequencies increase, both in the forward and in the backward sweeps (the latter to a lesser extent), decreasing the total gap amplitude G and increasing the peak table acceleration A and the stiffness of the bumpers B. As concerns the maximum values of normalized excursion of absolute acceleration, both in the forward and in the backward resonance condition, they increase with the acceleration A and the stiffness of the bumpers B, whereas they show, depending on the pair B-A, a partial or complete bell-shaped trend, decreasing the total gap amplitude G. In a dual manner, the maximum values of normalized excursion of relative displacement decrease decreasing G and increasing the peak table acceleration A and the stiffness of the bumpers B, both in the forward and in the backward resonance condition. In addition, for the higher values of acceleration (A2 and A3) and in correspondence with the smaller gaps (G1 and G2), the appearance of secondary resonances, of gradually increasing amplitude as the bumper's stiffness B increases, in the low frequency range was observed.

Based on the observation of the characteristics of the experimental PRCs, four scenarios were introduced, namely scenario S0 corresponding to the free flight condition; scenario S1 corresponding to the grazing condition; scenario S2 with PRCs characterized by the presence of only the primary resonance with right hysteresis; scenario S3 with PRCs with both the primary resonance with right hysteresis and the secondary resonance. These scenarios were investigated in more detail analysing phase portraits, Fourier spectra and time histories of relative displacement, absolute acceleration and relative velocity of the mass in steady-state condition.

The experimental investigation was followed by a numerical analysis conducted using a Simplified Nonlinear Model (SNM), that is a numerical model in which both the bumpers and the damper were modelled with a Kelvin-Voigt model, retaining the other nonlinearities which characterize the problem, namely the existence of clearances, the unilaterality of the contact and the occurrence of impact, which causes abrupt changes of stiffness and damping at the contact time. The use of a linear visco-elastic modeling of both damper and bumpers, despite its limitations, was satisfactory for the purposes of this study. Once the model parameters have been identified, it was possible to numerically reproduce, in a sufficiently accurate manner, the scenarios observed experimentally. It was observed that the SNM, despite its relative simplicity, can give quite satisfying results in good agreement with the experimental outcomes. It is able to reproduce both qualitatively and quantitatively the primary resonance and the downward jump, whereas it is not able to precisely capture other phenomena such as the frequency of the upward jump. A good agreement between experimental and numerical results was observed also in the phase portraits.

For this reason the SNM was used to integrate the experimental results and fill the void left by experimentation. In particular, further numerical investigations allowed to highlight the existence of more complex response scenarios (characterized by the existence of secondary regular resonances without hysteresis, secondary regular resonances with left hysteresis, secondary non-regular resonances without hysteresis, these last ones exhibiting pairs of quasi-periodic solutions of large amplitude and -starting by appropriate initial conditions- also periodic solutions of small amplitude), that could be obtained, for example, considering values of the total gap G smaller than those considered in the experimental laboratory campaign.

Finally, suitable dimensionless parameters, namely stiffness ratio, dimensionless relaxation time, dimensionless initial gap and damping factor of the SDOF system were introduced and the experimental results were framed in terms of these parameters. The transition to the dimensionless parameters allowed to reduce the number of parameters that influence the response of the system and, consequently, to synthesize in a single graph the results of both the experimental and numerical investigations, and to highlight how what matters are, not the values assumed by the individual involved physical parameters, but rather their relationships. This causes that the same scenario can be obtained with different combinations of the involved physical parameters.

Based on the numerical results, as a first future development of this work, there is the intention to investigate the possibility to experimentally regain the more complex scenarios obtained with the SNM. Furthermore, to fully capture, qualitatively and quantitatively, the main aspects of the response of the system, also a more refined nonlinear numerical model, that includes all the nonlinearities will be considered in future analysis.

## Conflict of interest

The authors declare that they have no conflict of interest.

## References

1. Ibrahim, R.A.: Vibro-Impact Dynamics: Modeling, Mapping and Applications. Lecture Notes in Applied and Computational Mechanics 43, Springer-Verlag, Heidelberg (2009)
2. Liu, Y., Wiercigroch, M., Pavlovskaia, E., Peng, Z.K.: Forward and backward motion control of a vibro-impact capsule system. Int. J. Nonlinear Mech. 70, 30–46 (2015)
3. Liu, Y., Pavlovskaia, E., Wiercigroch, M.: Experimental verification of the vibro-impact capsule model. Nonlinear Dyn. 83(1-2), 1029-1041 (2016)
4. Yan, Y., Liu, Y., Liao, M.: A comparative study of the vibro-impact capsule systems with one-sided and two-sided constraints. Nonlinear Dyn. 89(2), 1063-1087 (2017)
5. Gu, X.D., Deng, Z. CH.: Dynamical analysis of vibro-impact capsule system with Hertzian contact model and random perturbation excitations. Nonlinear Dyn. 92(4), 1781-1789 (2018)
6. Yan, Y., Liu, Y., Manfredi, L., Prasad, S.: Modelling of a vibro-impact self-propelled capsule in the small intestine, Nonlinear Dyn. 96(1), 123-144 (2019)
7. Divenyi, S., Savi, M.A., Wiercigroch, M., Pavlovskaia, E.: Drill-string vibration analysis using non-smooth dynamics approach, Nonlinear Dyn. 70(2), 1017-1035 (2012)
8. Liu X., Vlajic N., Long X., Meng G., Balachandran B.. Nonlinear motions of a flexible rotor with a drill bit: stick-slip and delay effects. Nonlinear Dyn. 72(1-2), 61-77 (2013)

9. Liu X., Vlajic N., Long X., Meng G., Balachandran B.: Coupled axial-torsional dynamics in rotary drilling with state-dependent delay: stability and control. Nonlinear Dyn. 78(3), 1891-1906 (2014)
10. Liu, Y., Páez Chávez, J., De Sa, R., Walker, S.: Numerical and experimental studies of stickslip oscillations in drill-strings. Nonlinear Dyn. 90(4), 2959-2978 (2017)
11. Vaziri, V., Kapitaniak, M., Wiercigroch, M.: Suppression of drill-string stick-slip vibration by sliding mode control: Numerical and experimental studies. Eur. J. of Appl. Math. 29(5), 805–825 (2018)
12. de Moraes, L.P.P., Savi, M.A.: Drill-string vibration analysis considering an axial-torsional-lateral nonsmooth model. J. Sound Vib. 438, 220–237 (2019)
13. Malhotra, P.: Dynamics of seismic impacts in base-isolated buildings. Earthq. Eng. Struct. Dyn. 26(8), 797-813 (1997)
14. Komodromos, P., Polycarpou, P.C., Papaloizou, L., Phocas, M.C.: Response of seismically isolated buildings considering poundings. Earthq. Eng. Struct. Dyn. 36(12), 1605–1622 (2007)
15. Polycarpou, P.C., Komodromos, P.: On poundings of a seismically isolated building with adjacent structures during strong earthquakes. Earthq. Eng. Struct. Dyn. 39(8), 933–940 (2010)
16. Polycarpou, P.C., Komodromos, P.: Earthquake-induced poundings of a seismically isolated building with adjacent structures. Eng. Struct. 32(7), 1937–1951 (2010)
17. Masroor, A., Mosqueda, G.: Experimental simulation of base-isolated buildings pounding against moat wall and effects on superstructure response. Earthq. Eng. Struct. Dyn. 41(14), 2093–2109 (2012)
18. Masroor, A., Mosqueda, G.: Impact model for simulation of base isolated buildings impacting flexible moat walls. Earthq. Eng. Struct. Dyn. 42, 357–376 (2013)
19. Mavronicola, E.A., Polycarpou, P.C., Komodromos, P.: Effect of Planar Impact Modeling on the Pounding Response of Base-Isolated Buildings. Front. Built Environ 2(11), 1–16 (2016)
20. Reggio, A., De Angelis, M.: Optimal design of an equipment isolation system with nonlinear hysteretic behavior. Earthq. Eng. Struct. Dyn. 42, 1907–1930 (2013)
21. Reggio, A., De Angelis, M.: Combined primary-secondary system approach to the design of an equipment isolation system with High-Damping Rubber Bearings. J. Sound Vib. 333, 2386–2403 (2014)
22. Sarebanha, A., Mosqueda, G., Kim., M.K., Kim, J.H.: Seismic response of base isolated nuclear power plants considering impact to moat walls. Nucl. Eng. Des. 328, 58-72 (2018)
23. Jankowski, R., Wilde, K., Fujino, Y.: Reduction of pounding effects in elevated bridges during earthquakes, Earthq. Eng. Struct. Dyn. 29(2), 195–212 (2000)
24. Guo, A.X., Li, Z.J., Li, H., Ou, J.P.: Experimental and analytical study on pounding reduction of base isolated highway bridges using MR dampers. Earthq. Eng. Struct. Dyn. 38(11), 1307-1333 (2009)
25. Hao, H., Bi, K.M., Chouw, N., Ren, W.X.: State-of-the-art review on seismic induced pounding response of bridge structures. J. Earthq. Tsunami 7(3), 1350019-1-1350019-19 (2013)
26. Anagnostopoulos, S.A.: Pounding of building in series during earthquake. Earthq. Eng. Struct. Dyn. 16, 443–456 (1988)
27. Polycarpou, P.C., Komodromos, P.: Numerical investigation of potential mitigation measures for poundings of seismically isolated buildings. Earthq. Struct. 2(1), 1–24 (2011)
28. Polycarpou, P.C., Komodromos, P., Polycarpou, A.C.: A nonlinear impact model for simulating the use of rubber shock absorbers for mitigating the effects of structural pounding during earthquakes. Earthq. Eng. Struct. Dyn. 42(1), 81–100 (2013)
29. Renzi, E., De Angelis, M.: Optimal Semi-active Control and Non-linear Dynamic Response of Variable Stiffness Structures. J. Vib. Control 11(10), 1253-1289 (2005)
30. Arena, A., Lacarbonara, W., Casalotti, A.: Payload oscillations control in harbor cranes via semi-active vibration absorbers: modeling, simulations and experimental results. Procedia Eng. 199, 501-509 (2017)
31. Johnson, K.L.: Contact Mechanics. Cambridge University Press, Cambridge, UK (1985)
32. Goldsmith, W.: Impact - The Theory and Physical Behaviour of Colliding Solids. Edward Arnold Ltd., London, England (1960)
33. Muthukumar, S., DesRoches, R.: A Hertz contact model with non-linear damping for pounding simulation. Earthq. Eng. Struct. Dyn. 35, 811-828 (2006)
34. Machado, M., Moreira, P., Flores, P., Lankarani, H.M.: Compliant contact force models in multibody dynamics: Evolution of the Hertz contact theory. Mech. Mach. Theory 53, 99–121 (2012)
35. Skrinjar, L., Slavič, J., Boltežar, M.: A review of continuous contact-force models in multibody dynamics. Int. J. Mech. Sci. 145, 171–187 (2018)
36. Flores, P., Machado, M., Silva, M., Martins, J.: On the continuous contact force models for soft materials in multibody dynamics. Multibody System Dynamics, Springer Verlag. 25, 357–375 (2011)
37. Flores, P., Lankarani, H.M.: Contact Force Models for Multibody Dynamics. Springer (2016)
38. Hertz, H.: Ueber die Berührung fester elastischer Körper. Journal für die reine und angewandte Mathematik. 91, 156–171 (1881)
39. Půst, L., Peterka, F.: Impact Oscillator with Hertz's Model of Contact. Meccanica. 38, 99–114 (2003)
40. Dubowsky, S., Freudenstein, F.: Dynamic Analysis of Mechanical Systems With Clearances - Part 1: Formation of Dynamic Model. J. Eng. Ind. 93(1), 305-309 (1971)
41. Khulief, Y.A., Shabana, A.A.: A continuous force model for the impact analysis of flexible multibody systems. Mech. Mach. Theory 22(3), 213-224 (1987)
42. Hunt, K., Crossley, E.: Coefficient of restitution interpreted as damping in vibroimpact. J. Appl. Mech. 42(2), 440–445 (1975)
43. Wagg, D.J., Bishp, S.R.: Chatter, sticking and chaotic impacting motion in a two-degree of freedom impact oscillator. Int. J. Bifurcat. Chaos 11(1), 57–71 (2001)
44. Wagg, D.J., Bishp, S.R.: Dynamics of a two degree of freedom vibro-impact system with multiple motion limiting constraints. Int. J. Bifurcat. Chaos 14(1), 119–140 (2004)
45. Rigaud, E., Perret-Liaudet, J.: Experiments and numerical results on non-linear vibrations of an impacting Hertzian contact. Part 1: harmonic excitation. J. Sound Vib. 265, 289–307 (2003)
46. Luo, G.W., Lv, X.H., Shi, Y.Q.: Vibro-impact dynamics of a two-degree-of freedom periodically-forced system with a clearance: Diversity and parameter matching of periodic-impact motions. Int. J. Nonlin. Mech. 65, 173–195 (2014)
47. Luo, G.W., Zhu, X.F., Shi, Y.Q.: Dynamics of a two-degree-of freedom periodically-forced system with a rigid stop: Diversity and evolution of periodic-impact motions. J. Sound Vib. 334, 338–362 (2015)
48. Luo, T., Wang, Z.: Periodically forced system with symmetric motion limiting constraints: Dynamic characteristics

and equivalent electronic circuit realization. Int. J. Nonlin. Mech. 81, 283–302 (2016)
49. Hao, Z., Cao, Q., Wiercigroch, M.: Two-sided damping constraint control strategy for high-performance vibration isolation and end-stop impact protection. Nonlinear Dyn. 86, 2129-2144 (2016). https://doi.org/10.1007/s11071-016-2685-5
50. Wang, J., Shen, Y., Yang, S.: Dynamical analysis of a single degree-of-freedom impact oscillator with impulse excitation. Adv. Mech. Eng. 9(7), 1-10 (2017). https://doi.org/10.1177/1687814017716619
51. Gritli, H., Belghith, S.: Diversity in the nonlinear dynamic behavior of a one-degree-of-freedom impact mechanical oscillator under OGY-base d state-feedback control law: Order, chaos and exhibition of the border-collision bifurcation. Mech. Mach. Theory 124, 1-41 (2018)
52. de S. Rebouças, G.F., Santos, I.F., Thomsen, J.J.: Unilateral vibro-impact systems Experimental observations against theoretical predictions based on the coefficient of restitution. J. Sound Vib. 440, 346–371 (2019)
53. Andreaus, U., De Angelis, M.: Nonlinear dynamic response of a base-excited SDOF oscillator with double-side unilateral constraints. Nonlinear Dyn. 84, 1447–1467, (2016)
54. Andreaus, U., Baragatti, P., De Angelis, M., Perno, S.: A Preliminary Experimental Study About Two-Sided Impacting SDOF Oscillator Under Harmonic Excitation. J. Comput. Nonlin. Dyn. 12, 061010 (2017)
55. Andreaus, U., Baragatti, P., De Angelis, M., Perno, S.: Shaking table tests and numerical investigation of two-sided damping constraint for end-stop impact protection. Nonlinear Dyn. 90, 2387–2421 (2017)
56. Andreaus, U., De Angelis, M.: Experimental and numerical dynamic response of a SDOF vibro-impact system with double gaps and bumpers under harmonic excitation. Int. J. Dynam. Control 7(4), 1278–1292 (2019)
57. Andreaus, U., De Angelis, M.: Influence of the characteristics of isolation and mitigation devices on the response of SDOF vibro-impact systems with two-sided bumpers and gaps via shaking table tests. Struct. Control. Health. Monit. e2517 (2020). https://doi.org/10.1002/stc.2517
58. Stefani, G., De Angelis, M., and Andreaus, U.: Experimental dynamic response of a SDOF oscillator constrained by two symmetrically arranged deformable and dissipative bumpers under harmonic base excitation. In: Lacarbonara W., Balachandran B., Ma J., Tenreiro Machado J., Stepan G. (eds) Nonlinear Dynamics and Control, 119–127. Springer, Cham (2020) https://doi.org/10.1007/978-3-030-34747-5_12
59. Stefani, G., De Angelis, M., Andreaus, U.: Experimental and numerical investigation of base isolated SDOF system impact against bumpers under harmonic base excitation. In: Eccomas Proceedia (COMPDYN 2019), 2, 3333–3343 (2020). https://doi.org/10.7712/120119.7150.19207
60. Stefani, G., De Angelis, M., Andreaus, U.: Experimental and numerical response analysis of a unilaterally constrained SDOF system under harmonic base excitation. In: Proceedings of XXIV AIMETA Conference 2019, (2020) in press
61. Naeim, F., Kelly, J.M.: Design of Seismic Isolated Structures: From Theory to Practice. John Wiley and Sons, Chichester, U.K. (1999)